DTU Nanotech
Department of Micro- and Nanotechnology

Master Thesis, s062075

Modeling of Cell Reactions and Advection-Diffusion Processes in Microfluidic Biochips

Kasper W. Lipsø

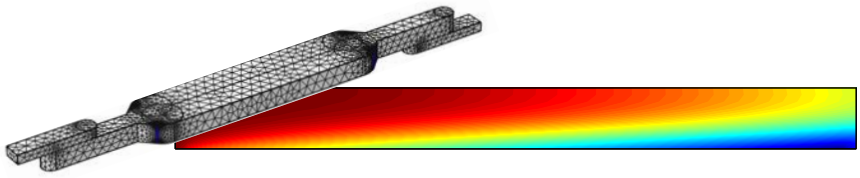

Supervisor: Henrik Bruus

Department of Micro- and Nanotechnology
Technical University of Denmark

4 July 2012

Front page illustration
The illustration on the front page shows the 3D geometry of the microchannel with a rough mesh. The color plot depicts the nutrition concentration in the reaction chamber from a 2D model.

Abstract

By moving experiments on stem cell differentiation from conventional setups to newly developed microfluidic devices, new knowledge about the differentiation process has been obtained. Data has indicated that a substrate secreted from a cell is essential for the differentiation process of the same cell and the neighboring cells.

The flow field of the microfluidic system is investigated by numerical simulations, where a full 3D model of the system is solved. The interaction between the diffusion and the advection of the secreted substrate and nutrition is examined, and central physical characteristics of the system are determined. After that, the 3D model is reduced to two dimensions, and the processes of diffusion and biochemical reactions are implemented. The first 2D model is an idealization, where the parameters have been scaled to let all processes act on the same timescale. The interplay between advection, diffusion and reactions is demonstrated. Next, a more realistic model is presented, where several parameters are estimated from experimental observations. It is tuned to fit new experimental results from the biologists in the group, and it is shown that basic characteristics of the system are in accordance with the model predictions.

Several experimental designs are then compared to the idealized or the more realistic model. First, the model is used to explain how the differentiation process decreases for large flowrates, because the factor is flushed away from the cells. Next, the differentiation dependence on the cell density is investigated, and it is shown that small intercellular distances can induce differentiation, because each cell is exposed to factor from nearby cells. The last example incorporates toxic elements in the infused medium, and thus provides an explanation of experiments where dilution of the medium has resulted in a higher differentiation rate.

Resumé

Ny viden om stamcelledifferentiering er blevet opnået ved at flytte eksperimentelle undersøgelser fra konventionelle opstillinger til nyudviklede mikrofluide anordninger. Data har indikeret at et stof udskilt fra en celle er essentielt for differentieringsprocessen i den samme og nærliggende celler.

Strømningsfeltet i mikrofluid-systemet undersøges ved numeriske simuleringer, hvor en fuld, tredimensionel model af systemet løses. Samspillet mellem diffusionen og advektionen af den udskilte faktor og næringsstoffer undersøges, og centrale fysiske størrelser af systemet udledes. Herefter reduceres 3D-modellen til to dimensioner, og diffusionsprocesser og biokemiske reaktioner implementeres. Den første model er idealiseret, så parametrene er skaleret så alle processer sker indenfor den samme tidsskala, og samspillet mellem advektion, diffusion og reaktioner demonstreres. Derefter præsenteres en mere realistisk model, hvor flere parametre estimeres ud fra eksperimentelle observationer. Den tilpasses ny eksperimentel data, og det vises at eksperimenter og simuleringer stemmer overens.

Herefter benyttes modellerne til at forklare observerede fænomener fra laboratoriet. Først hvordan differentieringsraten aftager ved store gennemløbshastigheder, fordi faktoren bliver skyllet væk fra cellerne. Derefter undersøges virkningen af celletætheden, og det påvises at lille afstand mellem celler kan inducere højere differentiering, fordi hver celle kan optage faktor udskilt fra omkringliggende celler. I det sidste eksempel implementeres giftige stoffer i baggrundsmediet. Det er en mulig forklaring på eksperimenter der viser, at differentieringen øges når mediet er blevet fortyndet.

Preface

This thesis is submitted in partial fulfillment of the requirements for obtaining the M.Sc. degree in Physics and Nanotechnology at the Technical University of Denmark. The work has been carried out under supervision of Professor Henrik Bruus, DTU Physics, with assistance from Ph.D. student Søren Vedel. The workload corresponds to 30 ECTS credits, and the project has been carried out from December 2011 to July 2012.

The project is a part of the ProCell project (Programmable Cell Chip: Culturing and Manipulation of Living Cells with Real-Time Reaction Monitoring), funded by NABIIT (2008-2012).

The work has been done in close collaboration with the Fluidic Array Systems and Technology (FAST) group at the Department of Micro- and Nanotechnology, Technical University of Denmark, under Associate Professor Martin Dufva and Ph.D. Mette Hemmingsen. All the experiments in this report have been made by Mette Hemmingsen.

The project is cross disciplinary, and it has been my task to develop a model that incorporates the advection, diffusion and reactions in a single chamber of the chip. My results and new ideas have been discussed at several ProCell meetings. Each time, I have brought and explained different new model inputs and the resulting predictions of my model. These have been debated, and new experiments suggested to determine which way the next step should go. Many times, new experimental results and conclusions have turned the preliminary assumptions around, and the set of variables has been extended or reduced. Moreover, the changes has often resulted in numerical breakdowns of the model solving, and relevant timescales and dimensionless numbers had to be recalculated to get the parameters straight and simulations running again. The models presented in this thesis are therefore the last ones in a long line of suggested models.

Though it has sometimes been frustrating that the basic concepts kept changing, the constant progression in the understanding of the biological processes has been very motivating. The cross-disciplinary group has been essential in getting where we are now, and I am glad to have been a part of the progress.

The outline of the thesis is briefly presented in the following:

In Chapter 1, the system is introduced, and preliminary biological results are presented. Background theory about the physics of the system is presented in Chapter 2, and the flow field is analyzed. In Chapter 3, the two dimensional advection-diffusion-reaction model is set up and analyzed. First in an idealized form, and later in a more realistic form.

The model is compared to experimental results in Chapter 4 and the project is summed up in a conclusion.

The main results of the experiments will be compared to the conclusions of this thesis in a publication in the near future, the manuscript is in preparation.

I would like to thank the members of the ProCell group, Søren Vedel, Mette Hemmingsen, Martin Dufva and Henrik Bruus for many fruitful discussions, and helping out with arising questions. Furthermore, I would like to thank the members of the Theoretical Microfluidics group for a great inspiring environment, where help is always near. In particular, great thanks to my supervisor Henrik Bruus, who has been extremely accessible throughout the project and has been a great inspiration in the understanding of physics, the art of scientific writing, and scientific work as a whole. It has been a pleasure.

At last I would like to thank my family and friends for their support throughout the project.

Kasper W. Lipsø
Department of Micro- and Nanotechnology
Technical University of Denmark
Kongens Lyngby, July 2012

Contents

List of Figures

List of Tables

List of symbols

Symbol	Description	Unit/value
$\equiv$	Equal to by definition	
$\sim$	Of the same order	
$\approx$	Approximately equal to	
$\propto$	Proportional to	
$\gg, \ll$	Much greater than, much smaller than	
$\cdot$	Scalar product	
$\times$	Cross-product or multiplication sign	
$\partial_i = \partial/\partial_i$	Partial derivative with respect to i	$[i]^{-1}$
$\boldsymbol{\nabla}$	Gradient vector operator	m^{-1}
$\boldsymbol{\nabla}\cdot$	Divergence vector operator	m^{-1}
$\boldsymbol{\nabla}\times$	Rotation vector operator	m^{-1}
∇^2	Laplacian scalar operator	m^{-2}
A	Cross-sectional area	m^2
a	Scaling factor for velocity field	m/s
$c\,(\boldsymbol{x}, t)$	Concentration field	m^{-3}
D	Diffusion coefficient	m^2/s
$d\,(\boldsymbol{x}, t)$	Differentiated cell concentration field	m^{-2}
D_h	Hydraulic diameter	m
D_d	Diffusion coefficient of differentiated cells	m^2/s
D_f	Diffusion coefficient of factor	m^2/s
D_l	Diffusion coefficient of lipids	m^2/s
D_n	Diffusion coefficient of nutrition	m^2/s
D_u	Diffusion coefficient of undifferentiated cells	m^2/s
$\boldsymbol{e}_\mathrm{i}$	Unit vector pointing in the i-direction	m
$\boldsymbol{F}$	Body forces	N
$\boldsymbol{F}_\mathrm{grav}$	Gravity forces	N
$f\,(\boldsymbol{x}, t)$	Factor concentration field	$\mathrm{mol}/\mathrm{m}^3$
f_0	Factor threshold concentration	$\mathrm{mol}/\mathrm{m}^3$
g	Gravitational acceleration	m/s^2

Continued on next page

Symbol	Description	Unit/value
h	Height of channel	m
h_{in}	Height of inlet channel	m
h_{rc}	Height of reaction chamber	m
$\boldsymbol{J}_{\text{r}}$	Reaction boundary flux	m^{-3}/s
k_{d}	Reaction rate constant of differentiated cell metabolism	s^{-1}
k_{l}	Reaction rate constant of lipid production	s^{-1}
k_{u}	Reaction rate constant of undifferentiated cell metabolism	s^{-1}
k_{ud}	Reaction rate constant of differentiation	$\text{m}^3/(\text{s}\cdot\text{mol})$
l	Lipid concentration	mol/m^3
l_{in}	Length of inlet channel	m
l_{rc}	Length of reaction chamber	m
L_{e}	Entrance length	m
M	Molecular mass	Da
m_{g}	Mass of glucose	kg
$\boldsymbol{n}$	Surface normal vector	m
n	Nutrition concentration	mol/m^3
n_0	Nutrition concentration in medium	mol/m^3
$\dot{N}_{\text{n}}$	Available amount of nutrition	mol
N_{v}	Number of vacuoles in reaction chamber	
Q	Mass flowrate	m^3/s
P	Channel perimeter	m
$p(\boldsymbol{x}, t)$	Pressure field	Pa
$p_{\text{hs}}(\boldsymbol{x}, t)$	Hydrostatic pressure field	Pa
$P\acute{e}$	Péclet number	
$P\acute{e}_{\text{s}}$	System Péclet number	
R	Reaction rate	$\text{s}^{-1}\text{m}^{-2}$
R_{l}	Reaction rate of lipid production	$\text{s}^{-1}\text{m}^{-2}$
R_{d}	Reaction rate of differentiated cell metabolism	$\text{s}^{-1}\text{m}^{-2}$
R_{u}	Reaction rate of undifferentiated cell metabolism	$\text{s}^{-1}\text{m}^{-2}$
R_{ud}	Reaction rate of differentiation	$\text{s}^{-1}\text{m}^{-2}$
Re	Reynolds number	
Re_{rc}	Reynolds number in reaction chamber	
Re_{in}	Reynolds number in inlet channel	
s	Measure of specific distance in calculations	m
T	Temperature	K
u	Undifferentiated cell concentration	m^{-2}
$\boldsymbol{v}$	Velocity field	m/s
v_{i}	Velocity in i'th direction	m/s
V_{l}	Total volume of lipids	m^3
v_{max}	Maximum speed	m/s
v_{mean}	Average speed	m/s
v_{v}	Volume of vacuole	m^3

Continued on next page

Symbol	Description	Unit/value
w	Width of channel	m
w_{rc}	Width of reaction chamber	m
x, y, z	Rectangular coordinates	m
α	Amount of nutrition consumed in one metabolism cycle	mol
β	Amount of factor consumed in differentiation of one cell	mol
Δp	Pressure difference	Pa
η	Dynamic viscosity	$\mathrm{Ns/m^2}$
ρ	Mass density	$\mathrm{kg/m^3}$
σ	Percentage of lipid filled area	%
τ_{adv}	Characteristic time of advection	s
τ_{diff}	Characteristic time of diffusion	s
τ_{reac}	Characteristic time of advection	s
φ	Energy density	J/kg
Ω	Domain	
$\partial\Omega$	Boundary of domain Ω	

Chapter 1

Introduction & Motivation

Lipid production is an important process in the human body. The lipid tissue is an important endocrine organ involved in energy homeostasis. Besides, adipocytes (fat cells) are necessary to restore soft tissue after an injury, and fat cell secreted paracrine factors have been shown to improve wound healing. Thus, knowledge about the processes involved can help us develop regenerative medicines. Similarly, controlling the lipid production can make us able to grow or restore fat tissue in selected areas of the body. Thus artificial protheses may be avoided. Nearly 5000 women in Denmark are diagnosed with breast cancer each year [1], and being able to generate new fat tissue after mastectomies would be of great value for these people.

Furthermore, understanding of the processes involved in fat production may help us to control body weight increase and be valuable in the growing challenge of obesity around the world.

1.1 Introduction to stem cell research

Adipose-derived stem cells (ASC) are able to produce fat tissue by lipogenesis. They can be extracted from liposuction aspirates, and by definition, they should be able to differentiate into osteoblasts (bone cells), chondrocytes (cartilage cells) and adipocytes (fat cells). The extraction process is shown in Fig. 1.1.

The process of differentiation into fat producing cells is a complicated process that is not fully understood. *Christancho & Lazar*[3] have proposed the model shown in Fig. 1.2. The mesenchymal stem cells (MSC), of which ASC is a subgroup, first turn into committed white preadipocytes after influence of miscellaneous signaling substrates detected by external receptors. From this stage, the cell can transform into a fat producing white adipocyte. In the last step, several adipocyte specific genes are expressed, and transcriptional cascades are essential in the process. When a cell has reached the state of white adipocyte, lipids can be accumulated. Paracrine/autocrine signaling is a general manner of cell-to-cell signaling. In our project, we have shown that this kind of signaling is involved in the differentiation of a population of adipose-derived stem cells into adipocytes upon culture in adipogenic medium. Some of the signaling factors are released to the

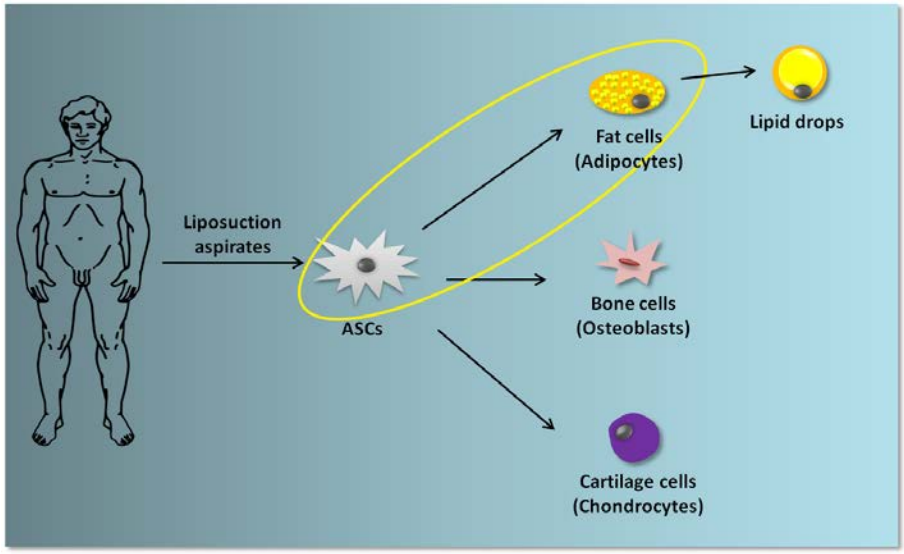

Figure 1.1: Adipogenic stem cells are extracted from liposuction aspirates. After isolation, they are differentiated into fat cells, that produce lipids. Figure from *Hemmingsen*[2].

external environment and then detected by the receptors in the cell membrane. Thus the differentiation is induced by *autocrine signaling*, where signaling substances are expressed and detected by the same cell. However, genes, factors etc. can also be detected by other cells in the proximity, *paracrine signaling*. Hence committed cells can induce commitment or differentiation of neighboring cells, creating a positive feed-back loop.

1.2 Microfluidics in biological research

Until recently, experiments on cell differentiation have been conducted *in vitro* in static cultures, where stem cells have been placed in well plates or cell culture flasks with large intercellular distances. Thus the signaling processes between neighboring cells have been very different from *in vivo* cell differentiation, where cells are surrounded by the extracellular matrix. By moving the experiments to microfluidic platforms, we can monitor the cell distance distribution, and the constant flow enables control or interruption of paracrine/autocrine signaling. *Blagovic et al.*[4] have been able to downregulate autocrine and paracrine signaling and thereby examine sufficiency of extracellular factors with their multiplex microfluidic platform.

Y.-H. Hsu et al.[5] used a microfluidic system to simulate a physiological environment. Thus it was possible to grow micro tissues of endothelial cells by letting medium perfusion act as the blood streaming in human blood vessels. Examples of the micro tissue is shown in Fig. 1.3

Another important feature of the microfluidic arrays is that several parallel experiments can be made, and high throughput can be obtained by combinatorics. *Gómez-Sjöberg*[6] managed to have 96 independent culture chambers on one chip and maintain cell viability

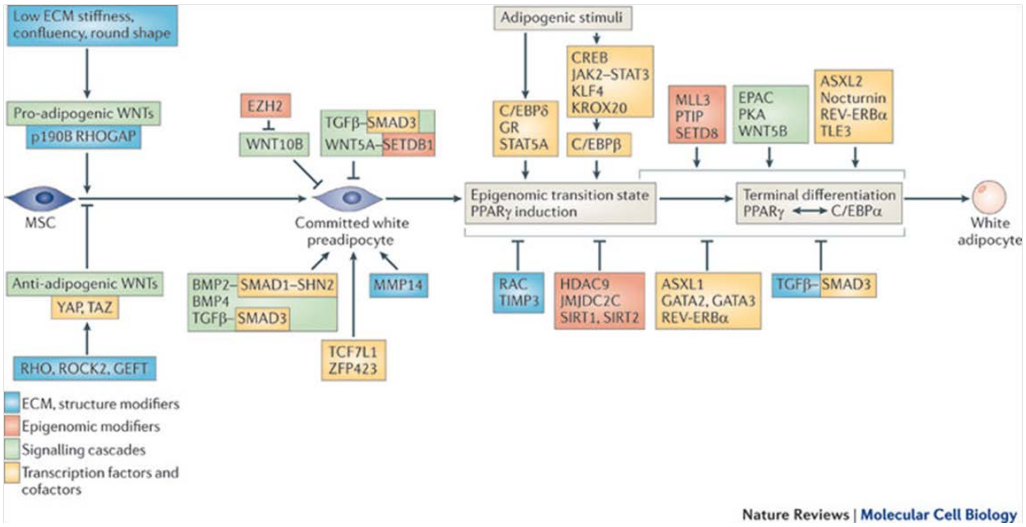

Figure 1.2: The differentiation of multipotent mesenchymal stem cells (MSCs) to mature adipocytes involves a complex integration of cytoarchitecture, signaling pathways and transcription regulators. Figure from *Christancho & Lazar*[3].

for weeks with endothelial cells.

Furthermore, biological experiments in microfluidic systems can be automated. Thus human mistakes can be eliminated, and the reproducability enhanced.

On the other hand, the transition from existing experimental setups to microfluidics propose several challenges. Biologists and technicians must learn how to use the new equipment. In addition, the new techniques must be better described, and the cellular environment in the microfluidic conditions understood. Moreover, many experiments must be remade in microfluidic systems to make sure that results from conventional setups can be transferred to the new technology. As an example, the ProCell chip is made in PMMA, and we must certify that the interaction with the chamber walls is similar to that of polystyrene walls, which is the typical material used in flasks, discs, etc.

1.3 ProCell platform

The ProCell platform makes it possible to track biological experiments in time. The platform is shown in Fig. 1.4. The flow from the reservoirs through the cell culture chip is pressure driven by peristaltic pumps [7]. The cell culture chip is placed in the center of the platform. The design of the chip is shown in Fig. 1.5. Stem cells are placed in reaction chambers, and can then be fed by infusing medium through the inlet channels. The chip is made from PMMA. Thus the experiment can be monitored visually. The entire platform fits in an incubator, where the appropriate conditions for temperature, humidity etc. can be obtained. The differentiation process usually takes some days or weeks, so the relevant dynamics can all be investigated by letting the experiment run for 21 days. The platform is put in a microscope every one or two days, where each of the reaction chambers is

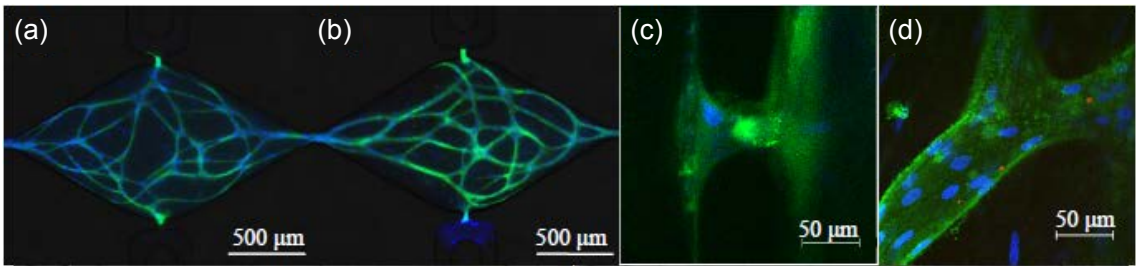

Figure 1.3: Images of micro tissues. (a-b) The cells have been stained with fluorescence so capillaries and nuclei light green and blue. (c) shows a capillary connecting to the side channel and (d) shows microbeads in a capillary network marked by red dots. Figure from *Y.-H. Hsu et al.*[5].

scanned.

Adipose-derived stem cells are hard to detect from visual monitoring due to their transparency. An example is shown in Fig. 1.6. The cells have grown for 21 days without differentiating. Thus they have grown on top of each other, and it is hard to see where one ends and another begins. It is much easier to monitor the lipid production. The lipids are emitted in vacuoles, whose outlines clearly distinguishes from cells and background. An example is shown in Fig. 1.7.

In conventional experiments with ASC differentiation, the medium is changed regularly, normally every four days. However, it has been observed [8] that the differentiation process was speeded up when only half the medium was exchanged every time. Therefore, medium from the cell culturing has been saved and added to the medium infused to some of the reaction chambers. To investigate a possible involvement of paracrine/autocrine signaling, medium collected from cells differentiating in a static cell culture, called *conditioned medium*, has been applied to the microfluidic perfusion experiments. The differentiation in the conditioned medium has been compared to the differentiation in the normal adipogenic differentiation medium.

The cells have been prepared in static cultures, where they were grown to a cell confluence of approximately $80 - 90$ %, i.e. until they filled $80 - 90$ % of the disk by area. The cell culture medium was changed to differentiation medium regularly to induce the differentiation. New medium was supplied every four days, where half of the conditioned differentiation medium (CM) was collected. The collected medium from days 4, 8, 12, and 16 after onset of differentiation was mixed in a 1:1 mixture with normal adipogenic differentiation medium, and later used in the solution infused to the microchannels under experiments.

In the experiments, the adipose-derived stem cells have been exposed to one of the following medium compositions:

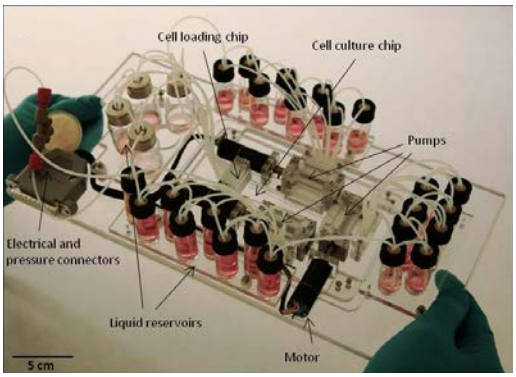

Figure 1.4: One version of the ProCell platform.

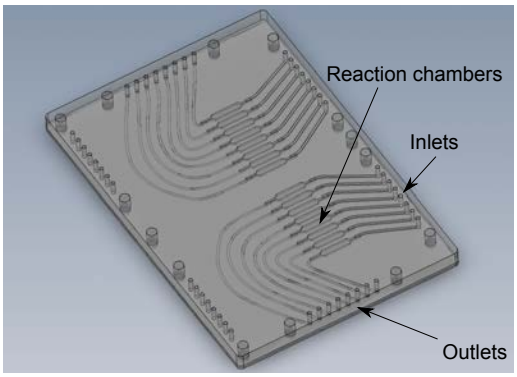

Figure 1.5: Design of the micro-channel system. The chip consists of 16 parallel micro chambers, each with separate inlet and outlet.

- **Adipogenic Medium (AM)**
  The medium consists of normal cell culture medium supplemented with substrates that induce cell differentiation, namely 0.5 mM IBMX (isobutyl-methylxanthine), 1 µM dexamethasone, 0.2 mM indomethacin, and 10 µg/mL insulin. These substances are collectively denoted *differentiation factors*.

- **AM + CM**
  AM has been prepared with 1.5 times the concentration of IBMX, dexamethasone, indomethacin and insulin normally used in AM. The concentrated AM was mixed 1:1 with conditioned medium.

- **AM diluted**
  The adipogenic medium diluted with normal cell culture medium without serum to give concentrations of one fourth of those in normal AM.

- **AM diluted + CM**
  The medium has been prepared as $1.5 \times \mathrm{AM} + \mathrm{CM}$, however adipogenic medium has been diluted four times before mixing with conditioned medium in the ratio 1:1.

A selection of experiments is presented in Fig. 1.8. In each column, a certain medium composition has been used, and the experiment has been running for 18 days. In each row, cells have been loaded with a certain cell concentration. The cell seeding density is hard to control when setting up the experiments. Cells are infused in the cell culture chip suspended in a solution. When the suspension has been infused with flowrate actuated by pumping, the flow is stopped while the cells sediment to the bottom of the reaction chamber. The cell density has then been estimated by manually counting of cells in a confined area. The images in Fig. 1.8 are selected from hundreds of experiments, because they contain several pieces of important information about the differentiation process.

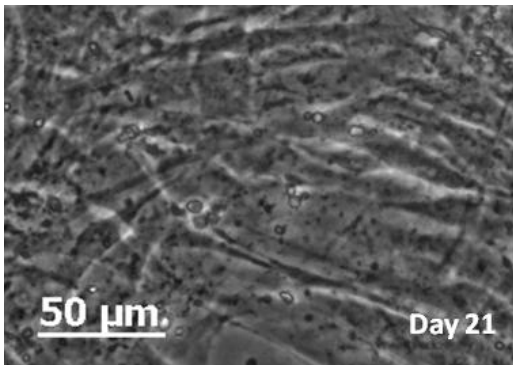

Figure 1.6: Negative control experiment. Adipogenic stem cells cultured in normal growth medium. No vacuoles are observed. The structure shows cells stacked in a matrix.

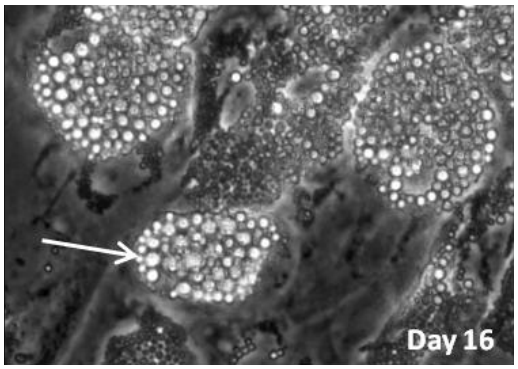

Figure 1.7: Lipid production by differentiated cells, where differentiation factors have been added to the medium. The arrow points out a vacuole. The scale is similar to that of Fig. 1.6.

Consider the first column of Fig. 1.8, where adipogenic medium has been supplied to the cells. With the lowest concentration of cells, $c_0 = 70$ cells/mm^2, only a few white dots are seen. Those are the few vacuoles that have been formed by differentiated cells, white adipocytes. The number and size of vacuoles are larger for $c_0 = 400$ cells/mm^2. The intercellular distance is now 5-6 times smaller. This phenomenon is even more obvious for $c_0 = 900$ cells/mm^2, where more cells have differentiated and started to produce vacuoles. Furthermore, the vacuoles are larger, so the differentiation has happened earlier than in the cases with low cell concentration. Since the conditions of these three experiments are identical except from the cell concentration, the differentiation of one cell must be influenced by the other cells.

We assume that this influence is caused by a transmitter substance - a small molecule that is released from cell. The molecule floats in the medium, and can then react with receptors in the membrane of the cell it came from or neighboring cells.

This assumption is supported when the addition of conditioned medium is considered. In the second column of Fig. 1.8, the images of such an experiment are shown. Again, the degree of differentiation and lipid production is increasing for increasing cell density. Furthermore, the area of lipids is larger than without conditioned medium. Recalling that conditioned medium has been collected from cells during their differentiation, it must have some of the proposed transmitter substance in it. Thus the differentiation process can start sooner when the medium has been added CM, and the number and size of the vacuoles is larger in column two than in column one. The effect of CM is not obvious for the low cell concentration. However, the differentiation of cells is stochastic, and a large number of differentiable cells is needed to make conclusions.

The area of lipids is shown in Fig. 1.9, where the total area of white lipids has been normalized to the total area of cells at the start of differentiation. It can qualitatively be

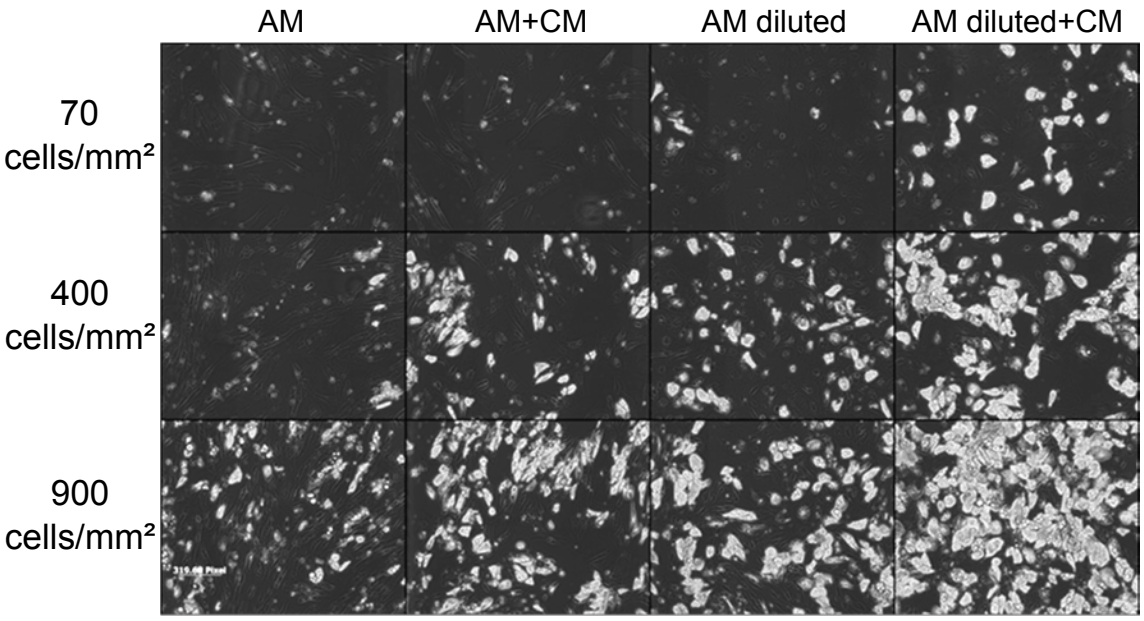

Figure 1.8: Images from samples of an experiment with different cell density or medium composition.

seen that the rate of differentiation has been increased for larger cell density and addition of conditioned medium, respectively.

It should be noted that the difference in the results of the first and the second column of Fig. 1.8 cannot be ascribed to the addition of CM only. The concentration of differentiation factors has been changed simultaneously. An experiment takes 21 days plus preparation, and the system must be taken out of the incubator and monitored several times along the way. Thus a limited number of experiments can be made. Therefore, we still have not investigated how much of the differentiation factors in the conditioned medium has been consumed by the cells in the culturing process. Instead, it is estimated that adding some extra differentiation factors approximately makes up for this. Hence the factor of 1.5 in the cases where CM is added.

Typical transmitter substances are cytokines, a group of small cell-signaling protein molecules. They are secreted by many different types of cells and are a category of signaling molecules used extensively in intercellular communication [9]. We will denote the concentration of the transmitter substance by the symbol f, and the substance will in the following be referred to as $factor$.

Transmitter substances are common as communication lines between cells. Recently, *Chandler et al.*[10] detected a similar factor from breast cancer cells that inhibits adipogenic differentiation while increasing proliferation, proangiogenic factor secretion, and myofibroblastic differentiation of ASCs.

Figs. 1.8 and 1.9 also give information about the effects of the concentrations of adipogenic factors in the medium. The medium is produced to induce cell differentiation. It

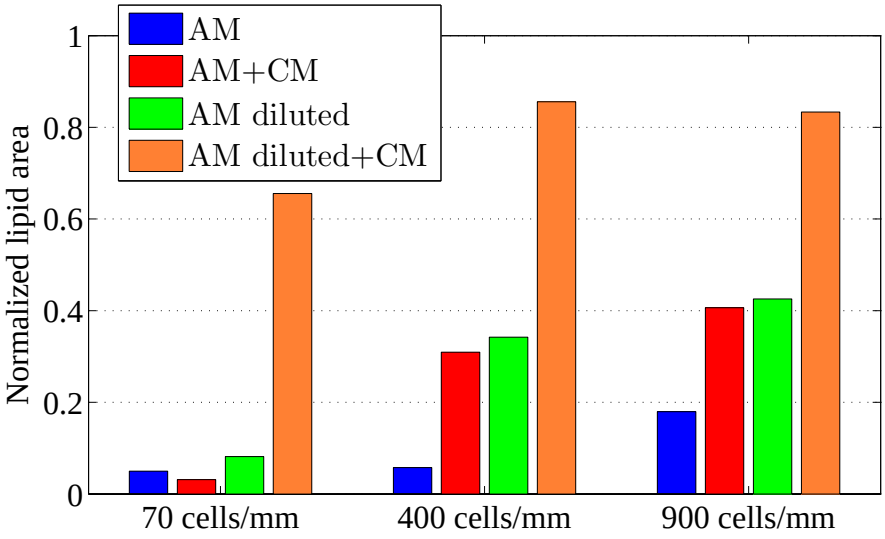

Figure 1.9: Representation of lipids 18 days after start of differentiation. The columns correspond to the area of lipids, normalized to the total area of cells.

is an aqueous solution containing more than 50 substances, including the 4 adipogenic factors, 21 amino acids, 10 vitamins and 12 inorganic salts [11]. A significantly larger degree of differentiation is obtained when the adipogenic medium is diluted to one fourth of the original concentration. The result is shown in the third column of Fig. 1.8. Comparing blue columns with green columns in Fig. 1.9, it is evident that a dilution of the adipogenic medium typically results in a twice as large area of lipids after the eighteen days. The same conclusion appears when conditioned medium has been added, where the orange columns are significantly higher than the red ones, corresponding to the fourth column of Fig. 1.8. A possible explanation is that the adipogenic medium contains some substrates that inhibit cell differentiation. A substrate with toxic properties to the adipogenic stem cells might thus cause some type of poisoning. The adipogenic medium has been optimized for cell differentiation in static cell culture, and therefore may be toxic in the conditions in the microfluidic perfusion system.

The image analysis used to get the data presented in Fig. 1.9 is simple, and only consider if each pixel of the microscope image represents lipids or not, and sums the area of the lipid. However, much more information about the formation and positions of vacuoles can be obtained by a more thorough image analysis. This is another important part of the ProCell project. Figs. 1.10 and 1.11 show some of the preliminary work in this discipline [12]. First, each vacuole is defined by grouping together white pixels that fit inside a confined, circular space. Next, the vacuoles are grouped by their distance to the center of the nearest cluster of vacuoles. Each of these groups corresponds to a single differentiated cell, marked by a identification color in Fig. 1.11. The area in Fig. 1.10 corresponds to around 1 % of the reaction chamber bottom area. Thus manual counting of vacuoles is very time consuming, and automation is needed. When the image analysis tools have

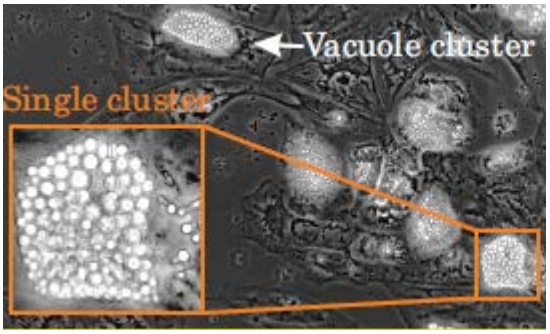

Figure 1.10: Microscope scan of the reaction chamber. Several circular vacuoles have emerges from each differentiated cell.

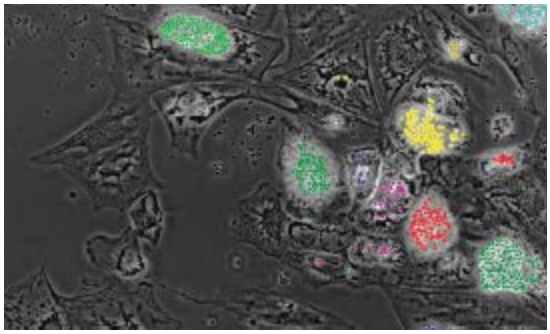

Figure 1.11: Each differentiated cell is defined, and the matching vacuoles are marked.

been developed further, we can get information about the positions of undifferentiated and differentiated cells, and determine the spatial distribution of the cells.

At this stage, however, we only know the overall area of lipids. Therefore, a discretized cell density function is not yet relevant, and this thesis will focus on flow characteristics and advection, diffusion and reactions in a reaction chamber with a continuous cell density function.

Chapter 2

Background theory

We want to set up a model that incorporates the essentials of the microfluidic stem cell differentiation experiments. The background assumptions and the equations of the system will be presented in this chapter.

2.1 Governing equations

The model is set up using continuum theory. Thus the concentrations of solutes and the density of cells are modeled as scalar fields. The flow of the medium is derived from the Navier-Stokes equation,

$$\rho\left(\frac{\partial \boldsymbol{v}}{\partial t} + \boldsymbol{v}\cdot\boldsymbol{\nabla}\boldsymbol{v}\right) = -\boldsymbol{\nabla}p + \eta\nabla^2\boldsymbol{v} + \boldsymbol{F} \tag{2.1}$$

where ρ is the density, $\boldsymbol{\nabla}$ is the vector differential operator, $\boldsymbol{v}$ is the velocity field, p is the pressure, η is the dynamic viscosity and $\boldsymbol{F}$ denotes body forces. It is assumed that the medium acts as a Newtonian fluid, so the viscosity is independent of velocity, i.e. η is constant. The Navier-Stokes equation describes the conservation of momentum. It is solved together with the continuity equation,

$$\frac{\partial \rho}{\partial t} + \boldsymbol{\nabla}\cdot(\rho\boldsymbol{v}) = 0, \tag{2.2}$$

which states that the flux into an arbitrarily shaped region is equal to the change in density. The medium used in the experiments is an aqueous solution, and it is assumed that is has hydrodynamic properties close to those of water. Thus assuming incompressibility of the medium, the continuity equation reduces to

$$\boldsymbol{\nabla}\cdot\boldsymbol{v} = 0. \tag{2.3}$$

Having established that the divergence of the velocity field is zero everywhere, we can determine the equation for the concentration fields. The processes affecting the concentration of substances in the channel involve advection, diffusion, and reactions. The rate

of change of the concentration scalar field c is

$$\frac{\partial c}{\partial t} = \boldsymbol{\nabla} \cdot (D \boldsymbol{\nabla} c) - \boldsymbol{\nabla} \cdot (\boldsymbol{v} c)\,, \tag{2.4}$$

where D is the diffusion coefficient. The terms in Eq. (2.4) denote contribution from diffusion and advection, respectively. The chemical and biological reactions in the present system take place on a boundary of the flow domain, and is therefore modeled as a flux $\boldsymbol{J}_{\mathbf{r}}$,

$$-\boldsymbol{n} \cdot \boldsymbol{J}_{\mathrm{r}} = R, \tag{2.5}$$

where $\boldsymbol{n}$ is the normal vector pointing into the domain we consider and R denotes the reactions. For reactions where c-substance is created, R acts as a source and is positive. For other reactions, where c-substance is being consumed, R acts as a sink, and is negative.

Gravity considerations

The medium, the solutes and the cells are all exposed to gravity forces. The gravity occurs in the last term of the Navier-Stokes equation as

$$\boldsymbol{F}_{\mathrm{grav}} = -\rho g \boldsymbol{e}_z. \tag{2.6}$$

The hydrostatic pressure is found by integration of Eq. (2.6) [13],

$$p_{\mathrm{hs}} = -\rho g z. \tag{2.7}$$

The total pressure in the channels is then

$$p_{\mathrm{tot}} = p_{\mathrm{hs}} + p, \tag{2.8}$$

where p is an auxiliary pressure. In the full Navier-Stokes equation, the hydrostatic pressure balances the gravitational term,

$$-\boldsymbol{\nabla} p_{\mathrm{hs}} = \rho g \boldsymbol{e}_z. \tag{2.9}$$

Thus we can ignore hydrostatic pressure and gravity in the flow computations, noting that the hydrostatic pressure must be added to the calculated pressure fields to get the actual pressure in the system. Furthermore, we can ignore gravity in the transport equation of the solutes, in that the substrates are assumed to be fully dissolved in the medium.

The stem cells are larger compounds, and definitely respond to gravity. However, we assume that the cells have already sediment when the model is initialized, and that they stay at the two dimensional chamber bottom. Thus gravity should not be considered for cells either.

2.2 Physical considerations

Reynolds number

We want to determine the Reynolds number for the reaction chamber and the inlet and outlet channels. The Reynolds number for a rectangular channel is determined from the hydraulic diameter D_h,

$$D_\mathrm{h} = \frac{4A}{P} = \frac{2hw}{h+w} \tag{2.10}$$

where A is the cross-sectional area of the inlet channel, P is the perimeter of the fluid/solid interface and h and w are the height and the width of the inlet channel, respectively.

The Reynolds number of a completely filled channel with laminar flow is

$$Re = \frac{\rho v D_\mathrm{h}}{\eta}, \tag{2.11}$$

where ρ is the density, v the velocity and η the dynamic viscosity.

The velocity is taken as the mean velocity in the channel, i.e. the flowrate Q divided by the cross-sectional area $A = hw$. The medium is an aqueous solution, and we can assume that $\rho = 1000$ kg/m^3. The Reynolds number is then given as

$$Re = \frac{2\rho Q}{\eta\,(h+w)}. \tag{2.12}$$

For typical values (20℃, water-like solution, high flow rate (500 nL/min)), the Reynolds number in the reaction chamber is

$$Re_\mathrm{rc} = 0.0083, \tag{2.13}$$

and the corresponding mean velocity in the flow direction is

$$v_\mathrm{mean} \approx 11.1\ \mu\mathrm{m/s}. \tag{2.14}$$

Similarly, the Reynolds number for flow in the inlet and outlet channels is

$$Re_\mathrm{in} = 0.017. \tag{2.15}$$

Thus we can consider laminar flow throughout the system.

Entrance length

The entrance lengths, i.e. the distance it takes to reach the fully developed velocity profile, can be determined as

$$L_\mathrm{e} \approx \max\left\{s, \frac{Re}{12}s\right\}, \tag{2.16}$$

where s is the smallest distance from the center of the channel to the side walls [14]. Thus we get for the inlet channel with $Re \ll 1$

$$L_\mathrm{e,in} \approx \frac{h}{2}. \tag{2.17}$$

For the design where the length of the inlet channel is $l_{\text{in}} = 1.0$ mm and the entrance length is
$L_{\text{e,in}} \approx 0.25$ mm, we can assume that the velocity profile is fully developed when entering the reaction chamber.

Characteristic time scales

The characteristic time scales of the system describe the time it takes each of the phenomena to take place. They must be determined and compared to each other to point out which processes are dominating the system, and which processes can be left out in the time windows we are considering.

The time it takes a particle to move from the inlet to the outlet of the reaction chamber by advection with a average horizontal velocity component v_{mean} of 11.1 µm/s (corresponding to a flowrate of $Q = 500$ nL/min), is

$$\tau_{\text{adv}} = \frac{l_{\text{rc}}}{v_{\text{mean}}} = 503 \text{ s}. \tag{2.18}$$

An estimate of the diffusion coefficient of a protein [15] is given as

$$D_{\text{pro}} = 8.34 \times 10^{-15} \frac{T}{\eta M^{1/3}}, \tag{2.19}$$

where temperature T, dynamic viscosity η and molecular mass M are given in units of kelvin, pascal-seconds and atomic mass units, respectively. Eq. (2.19) does not consider shape etc. of the protein, but has shown good correlation with experimental values.

We assume an aqueous solution at $T = 20$℃ with dynamic viscosity $\eta = 1.002 \times 10^{-3}$ Pa · s. Adipocyte differentiation has been associated with the protein Dickkopf-1 (Dkk1) [16], and we will consider it as a possible signaling molecule. It has a molecular mass of $M = 28672$ Da, hence we get the diffusion coefficient

$$D_{\text{pro}} = 8.0 \times 10^{-11} \ \frac{\text{m}^2}{\text{s}} \tag{2.20}$$

The time scale for the diffusion from the top of the channel to the cells at the bottom is [17]

$$\tau_{\text{diff,p}} = \frac{2h_{\text{rc}}^2}{D_{\text{pro}}} = 6250 \text{ s} \approx 12 \ \tau_{\text{adv}}. \tag{2.21}$$

Thus the characteristic time of diffusion is one order of magnitude larger that the characteristic time of advection.

Another important component of the medium is the dextrose, which act as the main resource of energy. Dextrose, or *D-glucose*, is smaller than the protein considered in Eq. (2.20), and thus have a larger diffusion coefficient of $D_{\text{dex}} = 6 \times 10^{-10}$ m^2/s [18]. The characteristic time of diffusion of nutrition is $\tau_{\text{diff,n}} = 833$ s, and thus comparable to the advection time from Eq. (2.18).

It is assumed that the characteristic time of the biochemical reactions is much smaller than the advection- and diffusion times, giving a large Damköhler number [19]. The characteristic time of a second-order reaction,

$$A + B \xrightarrow{k} A + C \tag{2.22}$$

is defined as

$$\tau_{\text{re}} = \frac{1}{B_0 k}, \tag{2.23}$$

where A, B and C are concentrations, B_0 is the initial concentration of compound B and k is the reaction rate constant. The time can be interpreted as the time it would take to consume all of the B compounds if the consumption rate was constant in time and equal to the initial rate. Assuming that glucose plays a dominating role in the metabolism of the cells, we will use the approximation that all of the relevant nutrients share properties with glucose. The concentration of glucose in the medium used to perfuse the system is $n_0 = 17.51$ mM. To match the diffusion- and reaction times, the reaction rate constants in a first model should be assigned the value

$$k = \frac{D}{2h_{\text{rc}}^2 n_0} \approx 0.01 \text{ M}^{-1}\text{s}^{-1}. \tag{2.24}$$

Péclet number

Another important number of the system is the Péclet number, which relates the rate of advection to the rate of diffusion. Usually the Péclet number is defined as

$$Pé = \frac{Lv}{D}, \tag{2.25}$$

where v is the speed and D is the diffusion coefficient. Using the length of the reaction chamber as the characteristic length scale L, the mean velocity in the reaction chamber for the characteristic speed v and the diffusion coefficient for nutrition, we get a Péclet number of $Pé = 103$.

However, a modulation of the Péclet number is required to describe the given system. We want to compare the diffusion of nutrition from the top to the bottom of the chamber to the advection from the inlet to the outlet of the chamber. This is the ratio that determines whether nutrition has time to diffuse to the bottom, where it is consumed, before leaving the chamber with the flow through the outlet. The vertical rate of diffusion can be expressed as $2D/h^2$, and the rate of nutrition advection through the channel with mean velocity as the characteristic velocity is lhw/Q. We then get

$$Pé_{\text{s}} = \frac{Qh}{2Dlw} \approx 2. \tag{2.26}$$

Thus the advection dominates the system at large flowrates, and the magnitudes of the two processes are comparable for smaller flowrates.

Nutrition availability

The velocity profile is examined in Section 2.3, where the velocity in the vertical center plane of the reaction chamber is determined to

$$v_x\left(y=0,z\right)=4v_{\max}\left[\frac{z}{h_{\mathrm{rc}}}-\left(\frac{z}{h_{\mathrm{rc}}}\right)^2\right]. \tag{2.27}$$

Now, assuming that the distance s traveled by diffusion of nutrition in the negative z-direction goes as

$$s=\sqrt{2D_{\mathrm{n}}t}, \tag{2.28}$$

we can track the z-position of a nutrition particle entering the reaction chamber at height z_0 to be

$$z_{\mathrm{p}}\left(t\right)=z_0-\sqrt{2D_{\mathrm{n}}t}. \tag{2.29}$$

The definitions of z_0 and the coordinate system are shown in Fig. 2.1. Inserting Eq. (2.29)

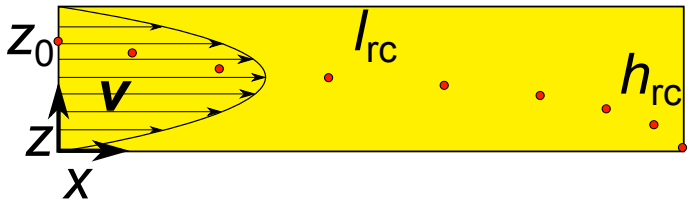

Figure 2.1: Tracing of nutrition particle entering the reaction chamber at height z_0 and exiting at height 0. Distances not to scale.

in Eq. (2.27), the velocity of a particle in the x-direction caused by advection is

$$v_{x,\mathrm{p}}\left(t\right)=\frac{4}{h}v_{\max}\left[z_0-\sqrt{2D_{\mathrm{n}}t}-\frac{1}{h}\left(z_0^2+2D_{\mathrm{n}}t-2z_0\sqrt{2D_{\mathrm{n}}t}\right)\right], \tag{2.30}$$

in rectangular coordinates x, y, z, where $v_{\max}$ is the maximum speed and h_{rc} is the height of the reaction chamber. Integration of Eq. (2.30) with respect to time gives us the distance travelled in the x-direction. Thus the distance L travelled in the time from $t=0$ to $t=T$ is

$$\begin{aligned} L &= \int_0^T v_{x,\mathrm{p}}\left(t\right)\,\mathrm{d}t \\ &= \frac{4}{h}v_{\max}\left[z_0T-\frac{2}{3}\sqrt{2D_{\mathrm{n}}}T^{3/2}-\frac{z_0^2}{h}T-\frac{D_{\mathrm{n}}}{h}T^2+\frac{4}{3}z_0\sqrt{2D_{\mathrm{n}}}T^{3/2}\right]. \end{aligned} \tag{2.31}$$

Now, the time before the particle reaches the chamber bottom is estimated as

$$\tau_{\mathrm{diff,n}}=z_0^2/\left(2D_{\mathrm{n}}\right). \tag{2.32}$$

For the standard conditions, the length travelled in the x-direction for a dextrose molecule is

$$L_{\mathrm{p}}=3.1\text{ mm}\approx 0.56l_{\mathrm{rc}} \tag{2.33}$$

before reaching the bottom. Thus all of the infused nutrition should be available to the cells at the bottom of the reaction chamber.

The maximum flowrate where all nutrition is available to the cells is found from Eq. (2.31). Setting $L = l_{\mathrm{rc}}$, we get a second order polynomial in z_0. The solutions are

$$z_0 = \frac{3h_{\mathrm{rc}}Tv_{\max} + 4\sqrt{2}T\sqrt{D_{\mathrm{n}}T}v_{\max} \pm \sqrt{-9h_{\mathrm{rc}}^2 l_{\mathrm{rc}}Tv_{\max} + 9h_{\mathrm{rc}}^2T^2v_{\max}^2 - 4D_{\mathrm{n}}T^3v_{\max}^2}}{6Tv_{\max}}, \tag{2.34}$$

where the second one (with a minus in place of $\pm$) is the physical solution.

The expression is valid for cases where a particle entering the chamber at the top has time to move through the entire chamber before reaching the bottom. Thus the limit where all infused nutrition is available to the cells is found with a maximum velocity $v_{\max,\mathrm{lim}}$ where the expression in the square root is zero for $z_0 = h_{\mathrm{rc}}$,

$$v_{\max,\mathrm{lim}} = \frac{3\left(3D_{\mathrm{n}}h_{\mathrm{rc}}^2 l_{\mathrm{rc}}T + 2\sqrt{2}h_{\mathrm{rc}}^3 l_{\mathrm{rc}}\sqrt{D_{\mathrm{n}}T}\right)}{4D_{\mathrm{n}}T^2\left(8h_{\mathrm{rc}}^2 - 9D_{\mathrm{n}}T\right)} = 40.2\ \mu\mathrm{m/s}, \tag{2.35}$$

or 1.79 times the standard maximum velocity. The flowrate scales linearly with the maximum velocity, therefore the flowrate limit where all infused sugar is available to the cells is

$$Q_{\mathrm{lim}} \approx 900\ \mathrm{nL/min}. \tag{2.36}$$

Similarly, the maximum entrance height of a nutrition particle reaching the cells is found by isolation of z_0 in Eq. (2.34), where $T \equiv z_0^2/(2D_{\mathrm{n}})$. The solution $z_0\left(v_{\max}\right)$ can be found in Appendix A. The function is plotted in Fig. 2.2, where the x-axis has been scaled from maximum velocity to flowrate in the unit of nanoliter per minute, the unit used in the laboratory. The curve begins in the limit where all infused nutrition is available to the cells, $z_0 = h_{\mathrm{rc}}$, as found in Eq. (2.36). As the flowrate is increased, the entrance height of a particle available to the cells decreases with a steep slope. In this domain of z_0, close to the top of the chamber, the horizontal velocity is small. On the contrary, the vertical diffusion velocity is independent of the horizontal velocity profile and flowrate. Thus a small increase in flowrate yields a large decrease in z_0. For larger values of Q, where $z_0 \to h_{\mathrm{rc}}/2$, the slope of the curve is less negative. The velocity profile $v_{\mathrm{x}}\left(z\right)$ is symmetric around $z_0 = h_{\mathrm{rc}}/2$. Therefore, the curvature or second derivative of the curve is small in this domain, and it is nearly linear. For extremely high flowrate, almost none of the nutrition can reach the cells, we get and $z_0 \to 0$ for $Q \to \mathrm{inf}$.

The function $z_0\left(Q\right)$ gives us some idea about how much of the infused nutrition that is available to the cells. However, the available amount depends both on the flowrate and the velocity profile. Thus the amount of available nutrition per second is

$$\dot{N}_{\mathrm{n}}\left(z_0\left(Q\right)\right) = n_0\int_0^{z_0} v_{\mathrm{x}}\left(z\right)\,\mathrm{d}z, \tag{2.37}$$

where n_0 is the initial nutrition concentration in the infused medium. The function is plotted in Fig. 2.3. The available nutrition amount $\dot{N}_{\mathrm{n}}$ increases as the flowrate is increased.

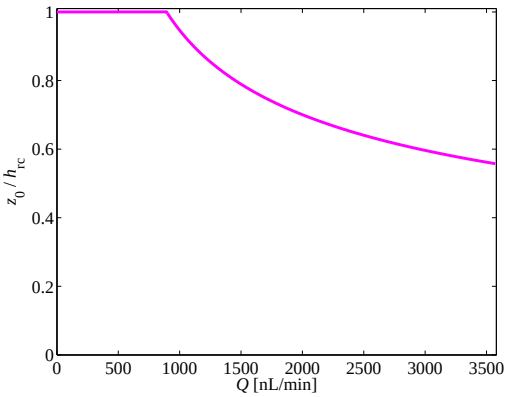

Figure 2.2: Entrance as a function of flowrate. z_0 defines the height of entrance for a nutrition particle ending up at the lower exit corner of the reaction chamber for a given flowrate.

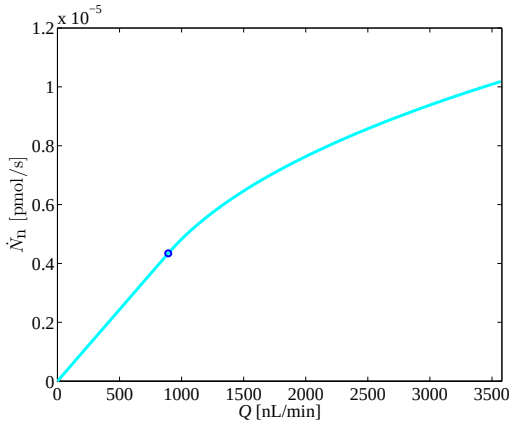

Figure 2.3: The amount of nutrition available as a function of flowrate. The blue circle marks the limit, where all nutrition potentially can reach the cells.

The ratio between available and infused nutrition is decreasing, thus the slope of the curve decrease.

An important feature of the Fig. 2.3 is that it is monotonically increasing. Parallel experiments in the *ProCell*-project where all conditions but the flowrate are identical has shown that high flowrates has inhibited cell differentiation. An assumption has been that some of the nutrition or differentiation factors has been flushed out with large flowrates, so that the net amount of available substrates has decreased. This assumption is here invalidated. The calculations have been carried out for dextrose with diffusion coefficient $D_n = 600\ \mu m^2/s$. The range of flowrates, velocities and distances are different for e.g. large proteins with smaller diffusion coefficients than that of dextrose. However, the proporties of the function of available x-substrate amount $\dot{N}_x(z_0(Q))$ are conserved, and the argument is valid for differentiation factors, salts, etc. as well.

The differentiation inhibition at large flowrates will be considered in Section 4.1.

2.3 Flow analysis

The model is set up with COMSOL Multiphysics 4.2a. We want to design a model that shows us the flow field in a full 3D geometry.

2.3.1 Geometry

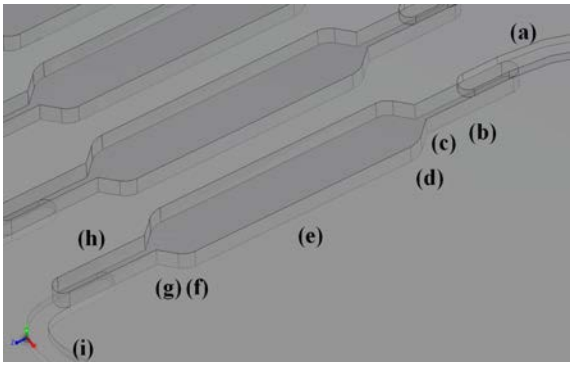

Figure 2.4: Design of a micro channel with inlet and outlet.

The design of the chamber is shown in Fig. 2.5. Fig. 2.6 shows the geometry implemented in COMSOL. The refinement of the mesh will be addressed in Section 2.3.4.
The design of the channel is shown in Fig. 2.4 and its dimensions are shown in Table 2.1.

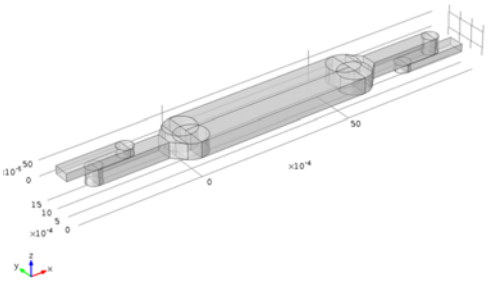

Figure 2.5: Geometry of the inlet, reaction chamber and outlet. It is build from rectangular boxes, circular prisms and trapezoidal prisms.

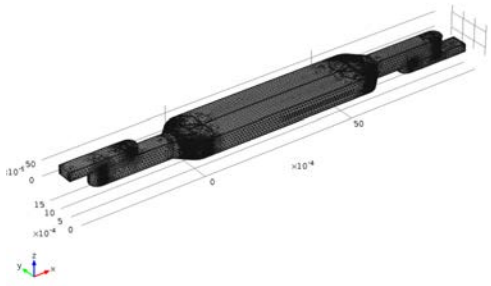

Figure 2.6: The mesh consists of 386699 elements. The largest distance between two nodes is 1 μm, and the mesh is finer around edges, corners etc.

A channel is composed in three vertical layers; a rectangular inlet channel in the upper layer (a), the reaction chamber in the middle (e) and an outlet channel in the lower layer. The reaction chamber is composed by a 'neck' (b) of same width as the inlet channel, a

widening trapezoidal prism (c), rounding 'shoulders' (d), the rectangular reaction chamber (e), another set of 'shoulders' (f), a narrowing (g) and a neck (h). The total length of the

Table 2.1: Dimensions of the micro chamber

Dimension	Symbol	Value
Inlet length	l_{in}	2 mm
Inlet width	w_{in}	500 µm
Inlet height	h_{in}	250 µm
Neck length	l_{ne}	250 µm
Neck width	w_{ne}	250 µm
Neck height	h_{ne}	250 µm
Shoulder radius	r_{sh}	500 µm
Reaction chamber length	l_{rc}	5.586 mm
Reaction chamber width	w_{rc}	1.5 mm
Reaction chamber height	h_{rc}	500 µm

selected geometry from inlet to outlet is $l_{\text{tot}} = 15.5$ mm.

2.3.2 Physical parameters

The equations of the flow is the incompressible Navier-Stokes equation for a Newtonian fluid, Eq. (2.1), and the continuity equation, Eq. (2.2). It is assumed that gravity is negligible, so no body forces are affecting the flow. The medium in the system has physical properties close to those of water. The applied values are shown in Table 2.2.

Table 2.2: Properties of water used in the flow analysis model

Property	Symbol	Value
Density	ρ	1000 kg/m^3
Dynamic viscosity	η	1.002×10^{-3} Pas

No-slip boundary conditions are applied on all solid walls.

2.3.3 Inlet velocity profile

The entrance length of the flow in the reaction chamber was addressed in Section 2.2. It is not possible to find an exact analytical solution to the velocity profile in the rectangular

inlet channel. *Bruus* [13] proposes a solution to laminar flow in microchannels having a rectangular cross-section with height h, width w, length L, dynamic viscosity η and pressure difference between inlet and outlet Δp, as a Fourier series,

$$v_x(y,z) = \frac{4h^2\Delta p}{\pi^3 \eta L} \sum_{i,\text{odd}}^{\infty} \frac{1}{i^3} \left[1 - \frac{\cosh\left(i\pi \frac{y}{h}\right)}{\cosh\left(i\pi \frac{w}{2h}\right)} \right] \sin\left(i\pi \frac{z}{h}\right). \tag{2.38}$$

As the flow through the system is more complicated than flow in a rectangular channel, we cannot use the magnitude of velocity given in Eq. (2.38). Thus we will only adopt the shape of the profile, i.e. the two brackets in the end of the expression. At first we will only consider the first term of the sum, $i = 1$. We then have

$$v_x(y,z) = a \left[1 - \frac{\cosh\left(\pi \frac{y}{h_{\text{in}}}\right)}{\cosh\left(\pi \frac{w_{\text{in}}}{2h_{\text{in}}}\right)} \right] \sin\left(\pi \frac{z}{h_{\text{in}}}\right). \tag{2.39}$$

where a is a scaling factor yet to be determined.

We will validate this velocity profile by comparing it to a numerical COMSOL model. The model is set up as a rectangular box with the dimensions of the inlet channel. The boundary conditions are a pressure of $p_{\text{in}} = 0.05$ Pa at the inlet and zero pressure at the outlet, and no-slip conditions on the other boundary planes. The inlet pressure has been taken from the front factor of Eq. (2.39). It will only be used to find the shape of the velocity profile, thus the order of magnitude is adequate for now.

The computed velocity field at the outlet is shown in Fig. 2.7 (a). Fig. 2.7 (b) shows the expression given in Eq. (2.39). It is very similar to the numerically determined flow field shown in Fig. 2.7 (a), and the difference plotted in Fig. 2.7 (c) support this impression. The first order analytical solution has been normalized by the maximum velocity. The maximum difference is 7.5 % of the maximum velocity. We can get an even better solution

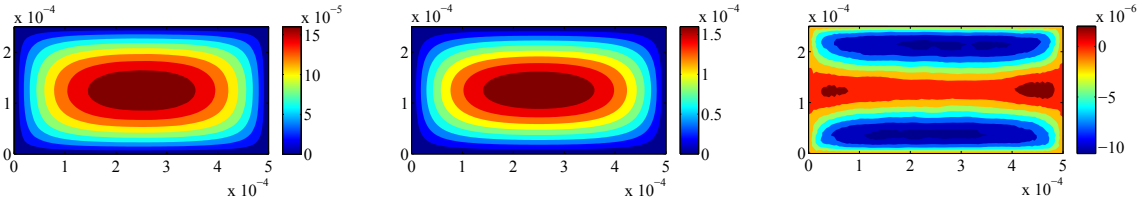

(a) (b) (c)

Figure 2.7: Velocity profile in the inlet channel. (a) shows the numerical result , (b) is the analytical approximation in Eq. (2.39) and (c) shows the numerical result minus the analytical result. Note that the colorbars of Figs. (a) and (b) span over a range ten times larger than that of Fig. (c).

by including the second term in the sum. Thus, to second order, we have

$$v_x(y,z) = a\left(\left[1 - \frac{\cosh\left(\pi\frac{y}{h}\right)}{\cosh\left(\pi\frac{w}{2h}\right)}\right]\sin\left(\pi\frac{z}{h}\right) + \frac{1}{27}\left[1 - \frac{\cosh\left(3\pi\frac{y}{h}\right)}{\cosh\left(3\pi\frac{w}{2h}\right)}\right]\sin\left(3\pi\frac{z}{h}\right)\right). \quad (2.40)$$

The second order contribution is shown in Fig. 2.8, and the difference between the second order approximation and the numerical result is shown in Fig. 2.9. The maximum difference is now 3.5 %. Accordingly, we will use Eq. (2.40) as the expression of the inlet velocity.

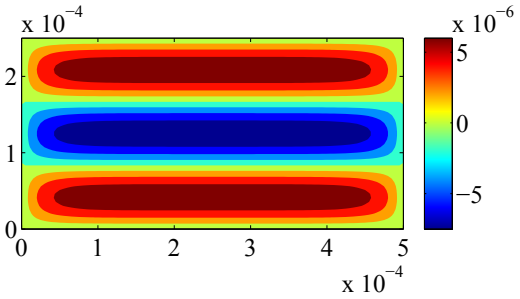

Figure 2.8: Second order contribution to the velocity profile in the inlet channel.

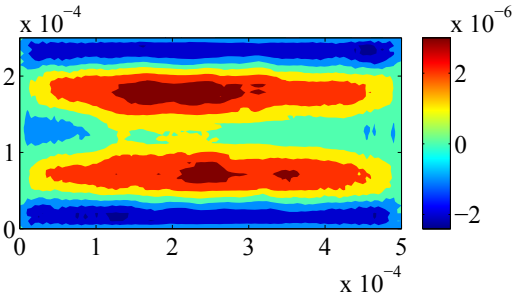

Figure 2.9: Difference between the second order approximation and the numerical result.

The inlet velocity profile is described more accurately by implementing more terms of the Fourier series. Series of up to five terms have been tested, but it turns out that the noise ín the resulting field from the meshing is a larger source of error, thus it makes no difference to use more than the first two terms.

On the other hand, we can model the inlet profile by a constant velocity profile throughout the inlet plane,

$$v_x(y,z) = \text{const.} \quad (2.41)$$

This boundary condition is in violence with the boundary condition of no-slip around the edges of the inlet. Therefore, this model takes extra computation time. The velocity profile in the end of the inlet with a flat entrance velocity profile is shown in Fig. 2.10. The velocity field is not identical to the previously computed fields. Thus, even after 2.5 times the entrance length L_e, the velocity profile has not developed fully. However, the velocity profile develops towards the fully developed profile as an exponential decreasing function of the length of the channel. Therefore, the entrance length is an estimate, that tells us when to expect a profile that is different from the fully developed profile by a small fraction only. This fraction is obvious from Fig. 2.11, where the velocity difference between flows with flat (Eq. (2.41)) and second order Fourier (Eq. (2.40)) profile boundary conditions is shown. Simulations with parabolic inlet velocity profiles have proved higher accuracy than the flat profiles, but not as accurate as Eq. (2.40). The second order Fourier approximation will therefore be used in the following simulations.

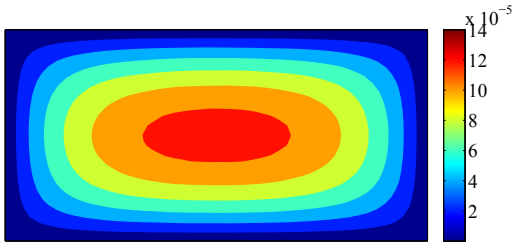

Figure 2.10: Velocity magnitude in the end of the inlet channel for a flat inlet velocity profile.

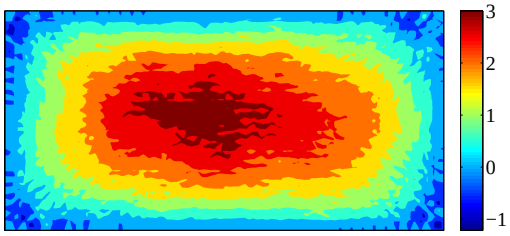

Figure 2.11: Velocity difference in the end of the inlet channel between flat and Fourier inlet velocity profile.

The flowrate through the system is found by integrating the expression in Eq. (2.40) over the cross-sectional areal A. We get

$$\begin{aligned} Q &= a \int \left(\left[1 - \frac{\cosh\left(\pi \frac{y}{h}\right)}{\cosh\left(\pi \frac{w}{2h}\right)} \right] \sin\left(\pi \frac{z}{h}\right) + \frac{1}{27} \left[1 - \frac{\cosh\left(3\pi \frac{y}{h}\right)}{\cosh\left(3\pi \frac{w}{2h}\right)} \right] \sin\left(3\pi \frac{z}{h}\right) \right) dA \\ &= a \left[\left(y - \frac{\frac{h}{\pi} \sinh \frac{\pi y}{h}}{\cosh \frac{\pi w}{2h}} \right) \left(-\frac{h}{\pi} \cos \frac{\pi z}{h} \right) + \frac{1}{27} \left(y - \frac{\frac{h}{3\pi} \sinh \frac{3\pi y}{h}}{\cosh \frac{3\pi w}{2h}} \right) \left(-\frac{h}{3\pi} \cos \frac{3\pi z}{h} \right) \right]_A \end{aligned} \tag{2.42}$$

Applying the boundary values in the vertical direction, $z = [0; h]$, we get

$$= a \left[\left(y - \frac{\frac{h}{\pi} \sinh \frac{\pi y}{h}}{\cosh \frac{\pi w}{2h}} \right) \frac{2h}{\pi} + \frac{1}{27} \left(y - \frac{\frac{h}{3\pi} \sinh \frac{3\pi y}{h}}{\cosh \frac{3\pi w}{2h}} \right) \frac{2h}{3\pi} \right]_{-w/2}^{w/2}. \tag{2.43}$$

Inserting the horizontal boundary values, $y = [-w/2; w/2]$, using that the hyperbolic sine is an odd function and the geometric relation $\frac{\sinh x}{\cosh x} = \tanh x$, we get

$$Q = a \left(\frac{2wh}{\pi} - \frac{4h^2}{\pi^2} \tanh\left(\frac{\pi w}{2h}\right) + \frac{2wh}{81\pi} - \frac{4h^2}{243\pi^2} \tanh\left(\frac{3\pi w}{2h}\right) \right) \tag{2.44}$$

The flowrate given in Eq. (2.44) yields the volumetric flowrate through the inlet channel with the profile given in Eq. (2.40) with an arbitrary velocity. With the dimensions of the inlet channel given in Table 2.1, we get the flowrate of $Q = a5.52198 \times 10^{-8}\text{m}^2$. For a typical flowrate of $Q = 500$ nL/s the factor a is

$$a = 0.000150912 \approx 0.151 \text{ mm/s}. \tag{2.45}$$

The flowrate, Eq. (2.44), per width is plotted in Fig. 2.12. A green circle marks the experimental setup, where the inlet aspect ratio is $AR = 2$. The flowrate per width is

$$\frac{Q}{w} = \frac{500 \text{ nL/min}}{0.5\text{mm}} = 1.67 \times 10^{-8} \text{ m}^2/\text{s} \tag{2.46}$$

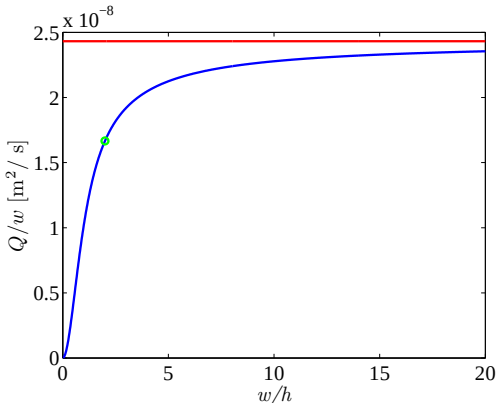

Figure 2.12: Flowrate per width through a rectangular channel with height $h = 0.25$ mm as a function of the width of the channel. The circle marks the experimental setup, and the red line describe the situation of flow between infinite plates.

in accordance with the figure. As the aspect ratio w/h increases, the flowrate per width saturates. Large aspect ratios look similar to the situation of flow between infinite plates. Here we can neglect the decrease in velocity due to the vertical side walls. Mathematically, the hyperbolic cosine functions with w as arguments increase rapidly, and leaves us with the velocity profile

$$v_x(y,z) = a\left(\sin\left(\pi\frac{z}{h}\right) + \frac{1}{27}\sin\left(3\pi\frac{z}{h}\right)\right). \tag{2.47}$$

We find the flowrate per width by integration over the cross sectional area A and dividing with the width w,

$$\begin{aligned}\frac{Q}{w} &= \frac{1}{w}\int a\left(\sin\left(\frac{\pi z}{h}\right) + \frac{1}{27}\sin\left(\frac{3\pi z}{h}\right)\right)\mathrm{d}A \\ &= a\int_0^h \sin\left(\frac{\pi z}{h}\right) + \frac{1}{27}\sin\left(\frac{3\pi z}{h}\right)\mathrm{d}z \\ &= a\left(\frac{2h}{\pi} + \frac{2h}{81\pi}\right)\end{aligned} \tag{2.48}$$

Using the height of the inlet channel, we get $Q/w = 2.43\times10^{-8}$ m^2/s. This value is shown as a red graph in Fig. 2.12.

Another relevant measure is the relation between maximum velocity in the reaction chamber and the flowrate. The maximum velocity is the velocity in the center,

$$v_{\max} = v_x(h/2,0) = \frac{4h^2\Delta p}{\pi^3\eta L}\sum_{n,\mathrm{odd}}^{\infty}\frac{1}{n^3}\left[1 - \frac{1}{\cosh\left(n\pi\frac{w}{2h}\right)}\right]. \tag{2.49}$$

The full expression of the flowrate is [13]

$$Q = \frac{h^3 w\Delta p}{12\eta L}\left[1 - \sum_{n,\mathrm{odd}}^{\infty}\frac{1}{n^5}\frac{192}{\pi^5}\frac{h}{w}\tanh\left(n\pi\frac{w}{2h}\right)\right]. \tag{2.50}$$

Substituting the expression of Q into Eq. (2.49) and calculating the sums for 1000 terms yields

$$v_{\max} = 2.7012 \times 10^6 \mathrm{m}^{-2} \cdot Q. \tag{2.51}$$

Thus the maximum velocity is $v_{\max} = 22.5$ µm/s, corresponding to twice the mean velocity in the reaction chamber.

No-slip boundary conditions on all other walls.

2.3.4 Verification of the 3D model

Cell Reynolds number

Assuming laminar flow, it must be confirmed that the flow is in the low Reynolds number domain, $Re \ll 1$. In the finite element, this should be valid for each element as well. The *cell Reynolds number* is defined as [20]

$$Re_{\mathrm{c}} = \frac{vh}{2\eta}, \tag{2.52}$$

where v is the velocity and h is the element size. The cell Reynolds number through the system is shown in Fig. 2.13. The largest cell Reynolds number are found in the inlet and outlet channels, where the flow velocity is largest,

$$Re_{\mathrm{c,max}} = 3 \times 10^{-3}. \tag{2.53}$$

Thus it is confirmed that the cell Reynolds number is small throughout the geometry, and it is safe to assume laminar flow. Having used the no-slip boundary condition, the velocity is zero along all outer walls, hence the cell Reynolds number is zero there.

Figure 2.13: Cell Reynolds number in the center plane of the full geometry. The darkest blue color corresponds to zero and the darkest red color has a value of $Re_{\mathrm{c}} = 3 \times 10^{-3}$.

2.3.5 Flow analysis results

We want to know the flow through the reaction chamber in particular. Consider first the velocity magnitude right after the expansion of the reaction chamber in Fig. 2.14. The flow profile already looks like flow in a rectangular channel, even though the inlet channel and the expansion of the reaction chamber is close nearby. This impression is supported by Fig. 2.15, which depict the x-component of the velocity field in the same plane. The two figures are almost identical, because the flow is almost only in the x-direction. Due to the widening of the channel, there is a flow away from the center of the channel. It can be seen in Fig. 2.16, where the y-component is shown. The fluid flows towards the side

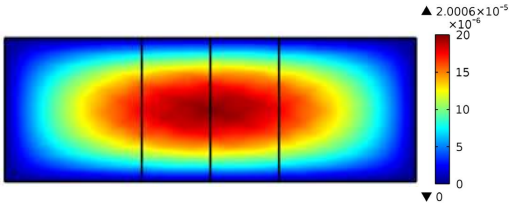

Figure 2.14: Velocity magnitude at the entrance of the reaction chamber, i.e. right after the expansion of the geometry.

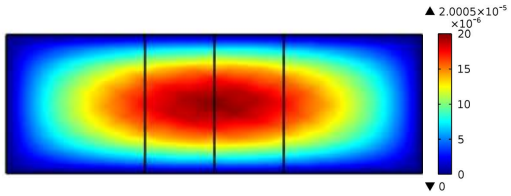

Figure 2.15: Velocity in the x-direction at the entrance of the reaction chamber.

walls to fill the entire chamber. The maximum of the y-component corresponds to 14 % of the maximum x-velocity.

The velocity component in the z-direction is practically zero. Hence the velocity component shown in Fig. 2.17 is noise from the numerical model.

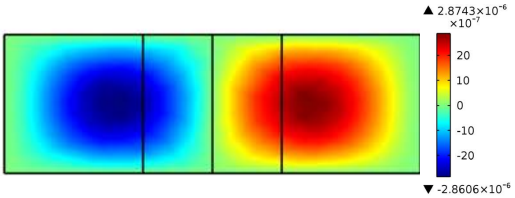

Figure 2.16: Velocity in the y-direction at the entrance of the reaction chamber.

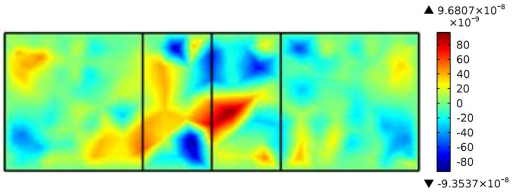

Figure 2.17: Velocity in the z-direction (vertical) at the entrance of the reaction chamber.

The velocity field in the entire geometry is summarized in Figs. 2.18 and 2.19. Fig. 2.18 shows the magnitude of velocity throughout the center of the reaction chamber, i.e. the plane $y = w_{\mathrm{rc}}/2$. The velocity is largest in the narrow inlet- and outlet channels, and almost zero in the corners of the geometry. Larger velocities are also detected in the "bottle necks", just before the widening to the reaction chamber. That is also evident from Fig. 2.19, where the velocity field in the center horizontal plane of the reaction chamber. Here, the inlet- and outlet channels cannot be seen, so the increasing velocity in the narrow regions of the "bottle necks" is obvious. The velocity field in the center rectangle, the reaction chamber, is nearly constant in x.

2.3.6 2D Velocity Profile

We also want to determine the flow in the vertical xz-plane in the center of the reaction chamber. Mathematically, the cosine hyperbolic function in Eq. (2.38) is a constant, and

Figure 2.18: Velocity magnitude throughout the system. The velocity is largest around the transitions from inlet to reaction chamber and from the reaction chamber to the outlet. The colorbar ranges from 0 to 1.4×10^{-4} m/s.

Figure 2.19: Top view of the velocity through the center of the reaction chamber. The colorbar ranges from 0 to 5.8×10^{-5} m/s.

the equation reduces to

$$v_x\left(y=0,z\right) = a \sum_{n,\text{odd}}^{\infty} \frac{1}{n^3} \sin\left(n\pi \frac{z}{h}\right), \tag{2.54}$$

where a is a constant with dimension of velocity. The Fourier sum reduces to a parabola [13], as with flow between infinite plates. In the 2D model considered in Chapter 3, the lower front corner of the reaction chamber is placed in the origin of the system. Thus the center of the parabola must be displaced with $h_{\text{rc}}/2$ in the positive z-direction, and the flow goes as

$$v_x\left(y=0,z\right) = 4v_{\max}\left[\frac{z}{h_{\text{rc}}} - \left(\frac{z}{h_{\text{rc}}}\right)^2\right], \tag{2.55}$$

where $v_{\max}$ is the maximum velocity in the center of the reaction chamber. The value of $v_{\max}$ is taken from Eq. (2.51), and the velocity profile is then fully described.

The flowfield defined by Eq. (2.55) and the corresponding flowfield from the 3D model are compared in Figs. 2.20 and 2.21The two flowfields resembles each other, even though there are differences, especially around the inlet and outlet. Therefore, we will ignore the change in shape of the channel when working with the velocity field in the reaction chamber, and use the analytic expression for the flow in the 2D model presented in Chapter 3.

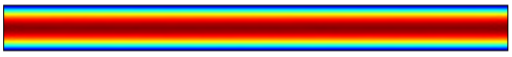

Figure 2.20: Ideal velocity magnitude throughout the center of the reaction chamber without inlet and outlet transitions. The darkest red color corresponds to 2×10^{-5} m/s, and the darkest blue color corresponds to zero velocity.

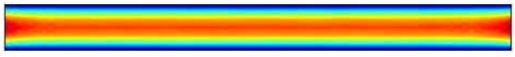

Figure 2.21: Velocity magnitude throughout the center of the reaction chamber in a full geometry model. Color codes as in Fig. 2.20.

2.4 Cell Reactions

The adipogenic medium flushing through the system contains several components such as salts, sugars, and adipogenic differentiation factors. It has been observed that adipogenic differentiation medium is crucial for cell differentiation [2]. Due to energy considerations, we must require that the chemical and biological processes involve nutrition (sugar) and amino acids. For simplicity, we will integrate all of these substances in the variable $n(\boldsymbol{x}, t)$.

In addition, it is known that the presence of cells act as a catalyst for the differentiation of cells. Assuming that the differentiation is influenced by a waste product of the metabolism of cells, we introduce the catalyst factor concentration field $f(\boldsymbol{x}, t)$.

The reaction chamber is loaded with cell loading densities ranging between 0.6×10^5 and 5.6×10^5 mL^{-1}, resulting in an actual cell seeding density in the order of 100 mm^{-1}. Thus the system contains maximum a few thousands of cells. However, the cell concentration will be treated as a continuous variable confined to the reaction chamber bottom.

The following four reactions will be considered in the model:

$$u + n \rightarrow u + f \tag{2.56a}$$
$$d + n \rightarrow d + f \tag{2.56b}$$
$$u + n + f \rightarrow d \tag{2.56c}$$
$$d + n \rightarrow d + l. \tag{2.56d}$$

Eq. (2.56a) is the metabolism of undifferentiated cells u, Eq. (2.56b) is the metabolism of differentiated cells d, Eq. (2.56c) is the differentiation of cells and Eq. (2.56d) is the productions of lipids l. Each of the reactions will be explained in the following.

We assume that undifferentiated cells u consume nutrition n for metabolism with a rate given by the reaction rate constant k_u. Incorporating the secretion of factor, the reaction equation for the metabolism of the undifferentiated cells u, is

$$u + \alpha n \xrightarrow{k_u} u + \beta f, \tag{2.57}$$

where α is the number of nutrition molecules and β is the number of product molecules f from one reaction cycle.

In an environment with limited resources, the metabolism will decrease. Furthermore, the cells have a maximum consumption rate when plenty of nutrition is available. These dynamics are modeled as a hyperbolic tangent function. Thus, for small nutrition concentrations, the rate of consumption is approximately proportional to the concentration of both cells and nutrition. For large nutrition concentration, only the cell concentration affect the rate. Thus the function resembles the rate of Michaelis-Menten kinetics, but without requiring a minimum concentration for the reaction to take place. The nutrition factor dependence can be interpreted as

$$n_0 \tanh\left(\frac{n}{n_0}\right) \approx \begin{cases} n & \text{if } n \ll n_0, \\ n_0 & \text{if } n \gg n_0. \end{cases} \tag{2.58}$$

The rate of the metabolic reaction of undifferentiated cells is given as

$$R_u = uk_u n_{0,u} \tanh\left(\frac{n}{n_{\mathrm{t,u}}}\right), \tag{2.59}$$

where $n_{\mathrm{t,u}}$ is the threshold nutrition concentration required for maximum consumption rate. This constant is used to normalize the argument of the hyperbolic tangent function, but is also used as a factor multiplied with the hyperbolic tangent function. Hence we get the appropriate unit of the k_u for a second order reaction rate constant. For small values of the argument $\frac{n}{n_{\mathrm{t,u}}}$, we get the expected second order reaction behavior, namely

$$R_u \approx uk_u n, \qquad n < n_{\mathrm{t,u}}. \tag{2.60}$$

Similarly, differentiated cells d consume nutrition corresponding to the reaction rate constant k_d. It is assumed that they, as the undifferentiated cells, secrete factor. Thus we get

$$d + \alpha n \xrightarrow{k_{\mathrm{d}}} d + \beta f, \tag{2.61}$$

where α and β are the same constants as in Eq. (2.59). Thus the relative amount of factor f produced by differential cells from nutrition consumed is now equal to that of the undifferentiated cells. However, the rate of the cycle can differ with a difference in the rate constants k_u and k_d.
The rate of the metabolic reaction of the differentiated cells is given as

$$R_d = dk_d n_{0,d} \tanh\left(\frac{n}{n_{\mathrm{t,d}}}\right), \tag{2.62}$$

where $n_{\mathrm{t,d}}$ is the nutrition concentration required for maximum consumption rate.

Another reaction we will consider in this model is the differentiation of cells. As a simple model we will assume that both nutrition and factor is required for a cell to differentiate, thus we get

$$u + \alpha n + \beta f \xrightarrow{k_f} d \tag{2.63}$$

where the reaction is irreversible. α and β are used for the proportion of nutrition and factor required in the reaction. This is an assumption, since we do not know how much is actually consumed for the differentiation of a cell. It is the best guess we have, and also fits our premise about keeping the number of variables and parameters low.
Again, assuming that the concentration of nutrition and factor is only affecting the reaction when there are limited amounts, the rate of differentiation R_{ud} is

$$R_{ud} = uk_{ud} n_{\mathrm{t,ud}} \tanh\left(\frac{n}{n_{\mathrm{t,ud}}}\right) f_0 \tanh\left(\frac{f}{f_0}\right) \tag{2.64}$$

where f_0 is a constant similar to $n_{\mathrm{t,u}}$ and k_{ud} is the reaction rate constant for cell differentiation.

The last reaction we will include in the model is the production of lipids from the differentiated cells. This is the variable we can observe visually from experiments. The concentration of lipid l is changing according to the reaction

$$d + \alpha n \xrightarrow{k_\mathrm{l}} d + \alpha l, \tag{2.65}$$

where α has been chosen for the number of nutrition- and lipid molecules in the reaction. It is thus assumed that one sugar molecule transforms to one lipid molecule.
The lipid production is dependent on a adequate level of nutrition, thus we get

$$R_l = dk_l n_{\mathrm{t,l}} \tanh\left(\frac{n}{n_{\mathrm{t,l}}}\right) \tag{2.66}$$

where k_l is the reaction rate coefficient and $n_{\mathrm{t,l}}$ is the level of nutrition required for full lipid production.

2.4.1 Undifferentiated cell concentration, u

We apply the no slip boundary condition for the velocity field on the channels walls. The cells only live on a boundary, the bottom of the chamber, and thus the concentration of cells is only changed through diffusion and differentiation. The governing equation for the concentration of undifferentiated cells u is

$$\frac{\partial u}{\partial t} = \boldsymbol{\nabla} \cdot (D_\mathrm{u} \boldsymbol{\nabla} u) - R_\mathrm{ud}, \tag{2.67}$$

where $\boldsymbol{\nabla}$ is the vector differential operator and D_u is the diffusion coefficient on the chamber floor.

A minor decrease in overall cell concentration has been observed experimentally. It is assumed that the decrease is caused by cell death. However, the effect is small and hence will not be included in the model.

We assume that the cells have already sediment when the model is initialized, and they are stuck to the two dimensional chamber bottom. Thus gravity should not be considered.

2.4.2 Differentiated cell concentration, d

Similarly the differentiated cells only live on the bottom of the chamber, and can only move by diffusion. Their governing equation is

$$\frac{\partial d}{\partial t} = \boldsymbol{\nabla} \cdot (D_d \boldsymbol{\nabla} d) + R_{ud}. \tag{2.68}$$

As for the undifferentiated cells, cell death is ignored.

2.4.3 Nutrition concentration, n

The nutrition is assumed to be diluted in the solution, hence we include the advection term defined as

$$\left(\frac{\partial n}{\partial t}\right)_{Adv} = -\boldsymbol{\nabla}\cdot(n\boldsymbol{v})\,, \tag{2.69}$$

where $\boldsymbol{v}$ is the flow velocity field and n is the nutrition concentration field. For incompressible fluids, Eq. (2.69) reduces to

$$\left(\frac{\partial n}{\partial t}\right)_{Adv} = -\boldsymbol{v}\cdot(\boldsymbol{\nabla} n)\,. \tag{2.70}$$

Including the diffusion, the equation for the rate of change of nutrition concentration in the bulk is

$$\frac{\partial n}{\partial t} = \boldsymbol{\nabla}\cdot(D_n\boldsymbol{\nabla} n) - \boldsymbol{v}\cdot(\boldsymbol{\nabla} n)\,. \tag{2.71}$$

The reactions of differentiation and metabolism of cells and differentiated cells and the production of lipids happens on the bottom boundary, where we get the flux

$$J_n = \alpha\left(-R_c - R_d - R_{ud} - R_l\right), \tag{2.72}$$

where the reaction rates R have been scaled with the parameter α, thus we obtain a decrease of α mol of nutrition for each reaction cycle.

2.4.4 Factor concentration, f

The concentration of factor f is free to move by diffusion and advection in the bulk of the channel. On the bottom of the chamber, it is produced from cell metabolism and consumed in the factor-induced differentiation of cells in Eq. (2.63). The equation for the rate of change of f in the bulk is

$$\frac{\partial f}{\partial t} = \boldsymbol{\nabla}\cdot(D_f\boldsymbol{\nabla} f) - \boldsymbol{v}\cdot(\boldsymbol{\nabla} f)\,. \tag{2.73}$$

The flux of factor f through the bottom boundary is the sum of the in-flux from factor production from cells and the out-flux from the consumption of factor in the differentiation of cells,

$$J_f = \beta\left(R_u + R_d - R_{ud}\right). \tag{2.74}$$

2.4.5 Lipid concentration, l

Assuming that the lipid released from the differentiated cells can diffuse along the bottom of the reaction chamber, the equation for the rate of change is

$$\frac{\partial l}{\partial t} = \boldsymbol{\nabla}\cdot(D_l\boldsymbol{\nabla} l) + \alpha R_l, \tag{2.75}$$

where D_l is the diffusion coefficient of the lipids.

2.5 COMSOL implementation

Preinstalled modules in COMSOL 4.2 let us compute the flow field and the mass flowrate of solutes in the bulk. The *Fluid Flow* module has a subgroup of modules, of which the *Single Phase Flow* is chosen. Here, the *Laminar Flow* module is selected, hence the equation systems are optimized for our simulations of flow in microfluidic systems. Thus we only supply the geometry and the coefficients for the Navier-Stokes and continuity equations. This is the module used in the flow analysis in Section 2.3.

Similarly, the mass transfer equations of the solutes in the bulk (nutrition and factor) are implemented with the *Transport of Diluted Species* function in the *Chemical Species Transport* module. Again, we supply the coefficients of the substrate properties (diffusion coefficient), and the boundary conditions. The mass transfer equations are coupled back to the velocity field derived with the *Laminar Flow* module.

The mass transfer equations of the substrates acting on the bottom boundary, however, has no preinstalled module. Thus the equations of motion must be implemented manually, through weak form modeling. In the following, the weak form of the advection-diffusion-reaction equation for undifferentiated cell density is derived. However, the cell live on the boundary layer with no flow, thus the advection is omitted.

The equation for the rate of change of undifferentiated cell concentration on the bottom of the channel was derived in Section 2.4.1 to be

$$\frac{\partial u}{\partial t} = \boldsymbol{\nabla} \cdot (D_{\mathrm{u}} \boldsymbol{\nabla} u) - R_{\mathrm{ud}} \tag{2.76}$$

where D_{u} is the diffusion coefficient for the cells and R_{ud} is the rate of differentiation. The first term on the right hand side is the diffusion of the cells, and the second term is the loss of undifferentiated cells due to differentiation.

Multiplying the right hand side with the test function $\tilde{u}$ and integrating over the surface Ω yields

$$\begin{aligned} &\int_{\Omega} \tilde{u} \boldsymbol{\nabla} \cdot (D_{\mathrm{u}} \boldsymbol{\nabla} u) - \tilde{u} R_{\mathrm{ud}} \mathrm{d}A \\ &= D_{\mathrm{u}} \int_{\Omega} \tilde{u} \nabla^2 u \mathrm{d}A - \int_{\Omega} \tilde{u} R_{\mathrm{ud}} \mathrm{d}A. \end{aligned} \tag{2.77}$$

The divergence operator is a linear operator. Thus we can derive the identity

$$\tilde{u} \nabla^2 u = \boldsymbol{\nabla} \cdot (\tilde{u} \boldsymbol{\nabla} u) - \boldsymbol{\nabla} \tilde{u} \cdot \boldsymbol{\nabla} u. \tag{2.78}$$

Inserting this expression in Eq. (2.77), we get

$$D_{\mathrm{u}} \int_{\Omega} \boldsymbol{\nabla} \cdot (\tilde{u} \boldsymbol{\nabla} u) - \boldsymbol{\nabla} \tilde{u} \cdot \boldsymbol{\nabla} u \mathrm{d}A - \int_{\Omega} \tilde{u} R_{\mathrm{ud}} \mathrm{d}A. \tag{2.79}$$

Using the divergence theorem, the first term can be converted to the line integral

$$D_{\mathrm{u}} \int_{\Omega} \boldsymbol{\nabla} \cdot (\tilde{u} \boldsymbol{\nabla} u) \, \mathrm{d}A = D_{\mathrm{u}} \int_{\partial \Omega} \tilde{u} \boldsymbol{\nabla} u \cdot \boldsymbol{n} \mathrm{d}L, \tag{2.80}$$

where $\boldsymbol{n}$ is the out pointing unit vector and L runs around the edge of Ω, $\partial\Omega$. The cells are constricted to the defined area, thus $\boldsymbol{\nabla} u = 0$ at the edge $\partial\Omega$. We can therefore ignore this term in the equation for the cell domain, and Eq. (2.79) reduces to

$$\int_{\Omega} -D_{\mathrm{u}} \boldsymbol{\nabla} \tilde{u} \cdot \boldsymbol{\nabla} u - \tilde{u} R_{\mathrm{ud}} \mathrm{d}A. \tag{2.81}$$

The final weak form equation in the domain where the cells live is found by taking the integrands, thus

$$\frac{\partial u}{\partial t} = -D_{\mathrm{u}} \left(\boldsymbol{\nabla} u \cdot \boldsymbol{\nabla} \tilde{u} \right) - \tilde{u} R_{\mathrm{ud}}. \tag{2.82}$$

The final weak form PDE for the domain to be implemented in COMSOL is

$$0 = D_{\mathrm{u}} * (-test(uTx) * uTx - test(uTy) * uTy) + test(u) * (-k_{\mathrm{u}} nu - ut), \tag{2.83}$$

where uTx and uTy denotes the x- and y-derivatives of u, respectively, and $test(u) = \tilde{u}$.

The equations for differentiated cell concentration d and lipid concentration l are derived equivalently.

Chapter 3

2D Advection-Diffusion-Reaction Model

In the models presented in the previous chapters, we have considered convection and diffusion in all three dimensions. However, the flow is nearly constant in the sideways y-direction in a large part of the domain, where the sidewalls of the channels do not affect the flow significantly. In addition, the diffusion in the z-direction is the only important diffusion to consider in the model. Thus we can reduce the flow domain to the vertical, two-dimensional xz-plane shown in Fig. 3.1.

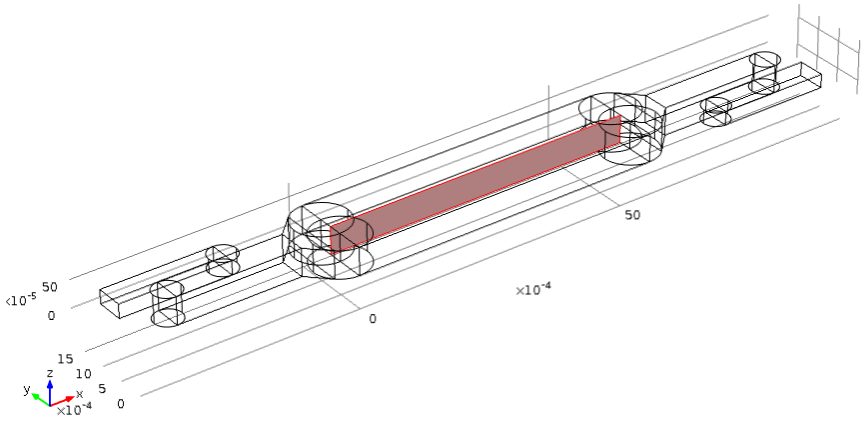

Figure 3.1: The highlighted vertical xz-plane is the domain of the system considered in the 2D model.

3.1 Idealized model for easy numerics

Initially, the model will be set up with parameters corresponding to comparable characteristic time scales. Thus the first step is an idealized model, where the terms in the equations for mass conservation will have comparable magnitudes, and we will be able to see the effects of advection, diffusion, and reactions in the results. Thus the time scales of the different processes are of comparable magnitudes. This is important in order to find numerical solutions spending a reasonable small amount of computation power. Realistic values will be considered and implemented in Section 3.2.

3.1.1 Geometry

The equations of mass conservation of nutrition and factor are solved in a vertical plane through the center of the reaction chamber with dimensions $l_{\mathrm{rc}} \times h_{\mathrm{rc}}$. The variables of undifferentiated and differentiated cells and lipids are constrained to the lower boundary of the domain. However, as COMSOL requires dirichlet boundary conditions for these variables on the horizontal boundary, the cells are restricted to the 98% center of the bottom between points 3 and 5 in Fig. 3.2. Thus no cells or lipids exist in the first and last 50 microns of the reaction chamber bottom. This is done for technical reasons, but is reasonable from a physical perspective as well.

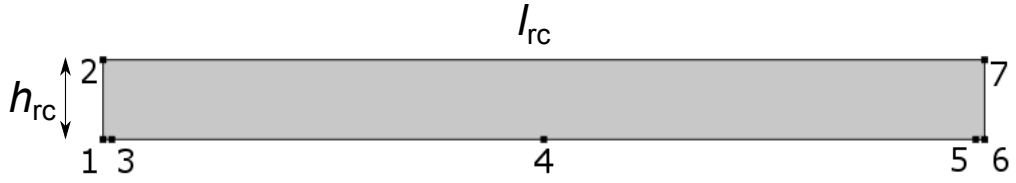

Figure 3.2: The boundaries around the reaction chamber are separated by points marked by the black squares.

3.1.2 Parameters and time scales

The first model can be thought of as an idealized model, where all of the considered elements are scaled to contribute to the result within same order of magnitude. Thus diffusion, reactions and advection will all take place on the same time scale, denoted τ. Furthermore, concentrations are chosen to be implemented as numbers per volume, $[c] = \mathrm{m}^{-3}$. An example is the nutrition concentration. In parallel, the initial concentration of undifferentiated cells on the two-dimensional bottom of the reaction chamber is set to $u_0 = 1\ \mathrm{m}^{-2}$. These concentration fields act linearly in the model, and can thus be scaled without loss of generality. Similarly, the scaling parameters of α and β are set to unity.

Velocity profile

Since we now consider the flow in the center of the reaction chamber only, the variations of the flow field in the y-direction are unimportant. Thus we use the velocity profile found in Eq. (2.55),

$$v_x(z) = 4v_{\max}\left[\frac{z}{h_{\mathrm{rc}}} - \left(\frac{z}{h_{\mathrm{rc}}}\right)^2\right], \tag{3.1}$$

where the origin is placed at point 1 in Fig. 3.2.

As the flow remains unchanged throughout the reaction chamber, we do not have to compute it from boundary conditions etc. and important computation power can be saved by implementing Eq. (3.1) in the entire geometry.

Advection time

The flowrate in the system is a parameter that we control externally of the system. It is a fixed value, an element which is held constant in the majority of the experiments. Furthermore, the flowrate is fully understood, and the parameters of density and viscosity is known with good precision. Therefore, the characteristic time of advection will be used as an intrinsic time scale, to which other relevant time scales are compared.

The time of advection can be defined as the time it would take to replace all of the medium in the reaction chamber with a flat flow profile, or, equivalently, how long it takes for an element of the medium to move from one end of the reaction chamber to the other by advection by mean velocity. In Section 2.2, we found that the characteristic time of advection is $\tau_{\mathrm{adv}} = 502.74$ s, or about 8 minutes.

Diffusion times

Advection is expected to dominate in the x-direction, i.e. along the channel. However, the flow is laminar and the movement of particles in the vertical z-direction is caused by diffusion. Choosing a characteristic time of diffusion to be equal to the advection time, we can compare Eqs. (2.18) and (2.21) to obtain

$$D_b = \frac{Qh_{\mathrm{rc}}}{2l_{\mathrm{rc}}w_{\mathrm{rc}}} \tag{3.2}$$

as a usable value of the diffusion coefficient of components in the bulk, namely nutrition and factor. Using the above expression, we obtain $D_b = 2.5 \times 10^{-10}$ m^2/s, or around three times larger than that of the protein Dkk1 estimated in Eq. (2.20).

Though the cells experimentally has proved to stick to the bottom of the channel, we will assume that they show a random-walk behavior on a small scale. This diffusion on the bottom surface will be exaggerated in the first model, so the characteristic time will match that of the other processes.

The relevant diffusion is along the flow direction, thus the important length scale is the length of the reaction chamber, l_{rc}. Following the practice of Eq. (3.2), a qualified

value of the diffusion coefficient for surface diffusion is

$$D_b = \frac{Q l_{\mathrm{rc}}}{2 h_{\mathrm{rc}} w_{\mathrm{rc}}}. \tag{3.3}$$

We get $D_s = 3.1 \times 10^{-8}$ m^2/s. Though exaggerated and thus a bit artificial, this is the diffusion to be used in the first model for the substrates on the bottom, i.e. cells and lipids.

Reaction times

Assuming that there is an abundance of nutrition, the nutrition factors can be omitted in the reaction rate expressions. Noting that the reaction rate constants k_{u}, k_{d}, k_{ud} and k_{l} then have another definition and unit, the reaction rates are

$$R_{\mathrm{u}} = k_{\mathrm{u}} u \tag{3.4a}$$
$$R_{\mathrm{d}} = k_{\mathrm{d}} d \tag{3.4b}$$
$$R_{\mathrm{l}} = k_{\mathrm{l}} d \tag{3.4c}$$
$$R_{\mathrm{ud}} = k_{\mathrm{ud}} f_0 u \tanh\left(\frac{f}{f_0}\right) \tag{3.4d}$$

where all rates have the dimension of $[R] = \mathrm{s}^{-1}\mathrm{m}^{-2}$. Thus the rate constants of k_{u}, k_{d} and k_{l} have dimensions of inverse time, and the corresponding time scales become

$$\tau_{\mathrm{r,u}} = \frac{1}{k_{\mathrm{u}}} \tag{3.5a}$$
$$\tau_{\mathrm{r,d}} = \frac{1}{k_{\mathrm{d}}} \tag{3.5b}$$
$$\tau_{\mathrm{r,l}} = \frac{1}{k_{\mathrm{l}}}. \tag{3.5c}$$

The cell differentiation, Eq. (3.4d), is a second order reaction. Therefore, a measure of the factor concentration is included in the function of characteristic time. Assuming that factor concentrations larger than the threshold value of f_0 are typical in the system, the time scale of differentiation is

$$\tau_{\mathrm{r,ud}} = \frac{1}{f_0 k_{\mathrm{u}}}. \tag{3.6}$$

Now, defining the reaction rate coefficient from Eqs. (3.5a) and (3.6) with the condition that $\tau_{\mathrm{r}} = \tau_{\mathrm{adv}}$, we expect to see the effects of all reactions in the results.

Furthermore, the constant f_0 should be estimated so that both situations with abundance of factor and situations with factor as the limiting resource for cell differentiation. The sum of the concentration of undifferentiated and differentiated cells is constant. Thus the total amount of factor released from their metabolism over the time τ is

$$n_{\mathrm{f}} = \beta u k_{\mathrm{u}} l_{\mathrm{rc}} w_{\mathrm{rc}} \tau, \tag{3.7}$$

where $l_{\mathrm{rc}} \times w_{\mathrm{rc}}$ is the area of the reaction chamber bottom. Using the characteristic time of advection for τ and recalling that $k_{\mathrm{u}} \equiv 1/\tau_{\mathrm{adv}}$, the non-dimensional concentration in the reaction chamber of factor secreted from cells is

$$f_{\mathrm{sec}} = \frac{\beta u}{h_{\mathrm{rc}}}, \tag{3.8}$$

or 2000 m^{-3}. However, much of the factor is consumed for cells differentiation as well as led out of the channel by advection. Therefore, a value of $f_0 = 20\ \mathrm{m}^{-3}$ is used in the idealized model.

The nutrition dependence was taken out of the model because abundance was assumed. The consumption of nutrition is assessed anyway. Thus the rate of differentiation is implemented as a nutrition flux out of the flow domain through the lower boundary. An arbitrarily chosen value of $\alpha = 10^{-4}$ mol is consumed every time a cell differentiates. The glucose concentration of $n_0 = 17.51$ mM from the medium used in experiments is assigned at the inflow.

3.1.3 Meshing and Convergence Analysis

The mesh of the geometry is shown in Fig. 3.3. It has been defined as a free triangular mesh, where the largest element side length corresponds to one percent of the length of the reaction chamber. This setting is defined as *extremely fine* in COMSOL Multiphysics. Thus there is a minimum of 100 elements along the top and bottom boundary. With a finer meshing around the corners, that corresponds to 2216 triangular elements. This refinement has proved adequate for most investigations, and the simulation can be run in seconds or minutes on an ordinary pc. For larger simulations with more varying conditions in the cell layer, the boundary layer around the bottom boundary should be refined further, but it has not been necessary in for these investigations. The reduction from three to two

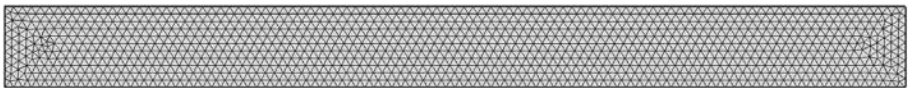

Figure 3.3: The geometry is meshed with a free triangular mesh.

dimensions has decreased the degrees of freedom (DoF) by orders of magnitude. The DoF depends partly on the meshing type and even more on the shape functions selected and the number of dependent variables from the different physics. The solution time of the model is shown for 10 different meshes in Table 3.1. The model has been solved with the COMSOL MUMPS solver for the dependent variables, namely the u, d, n, f and l fields, and use the transient equations for 100 time steps between 0 and 1000 s. All simulations has been done on a 6 GB RAM pc with Inter(R) Xeon(R) CPU processor of 3.07 GHz. The solution times are not direct measures of the computation power, but rather indications.

The refinement of the mesh has been exaggerated in the first mesh of the table. The solution of this model is used as a benchmark, to which the lower refinement mesh models

Table 3.1: Degrees of freedom (DoF) and solution times for different choices of number of elements (NoE).

Tag	**NoE**	**DoF**	**Solution time [s]**
Over refined	248740	256805	361
Extremely fine	2216	3027	6
Extra fine	638	1070	5
Finer	229	497	3
Fine	171	377	4
Normal	140	329	3
Coarse	117	271	4
Coarser	66	189	4
Extra coarse	48	155	4
Extremely coarse	34	123	3

are compared. The largest distance between two elements is 0.1 % of the length of the reaction chameber, resulting in hundreds of thousands of elements and DoF. The other nine meshes have been set up with COMSOL preinstalled settings ranging from *extremely fine* to *extremely coarse*. Though the number of elements ranges from 34 to 2216 in these meshes, the simulations all takes between 3 and 6 second. Hence the *extremely fine* mesh of Fig. 3.3 is used in the following simulations.

The lipid production is a good measure of the precision of the model for a given DoF. It is the last step in the reaction cycle, and thus depends on all the previous reactions, namely the factor secretion and the differentiation of cells. By integrating the lipid density along the bottom of the reaction chamber, we get one parameter Lp that describes the system. It is not dependent on a single node; instead the integration assures that the measure is a spatial average. The unit of Lp is m^{-1}, thus by multiplication with the width of the reaction chamber, w_{rc}, the total number of lipids in the system is determined. The value of $Lp\,(t)$ is plotted in Fig. 3.4 for the ten meshes of Table 3.1. The overall lipid production is almost the same, and the curves overlap. Thus even the mesh consisting of only 34 elements compute a satisfying computation of the total lipid production. However, focusing on the integration of lipid at time $t = 1000$ s only, the imprecision is pronounced. The $Lp\,(1000\ \mathrm{s})$ is plotted in Fig. 3.5, where the x-axis representing the number of elements is logarithmic to show all the values of Table 3.1. The value of produced lipids has been normalized with the computed lipid production of the over refined mesh model. It is obvious that the low numbers of elements yield some imprecision, and that the system is well described with the *extremely fine* mesh setting, the second last mark.

The imprecision can also be monitored by considering the lipid production over time, normalized by the over refined mesh model. The result is shown in Fig. 3.6. All of the

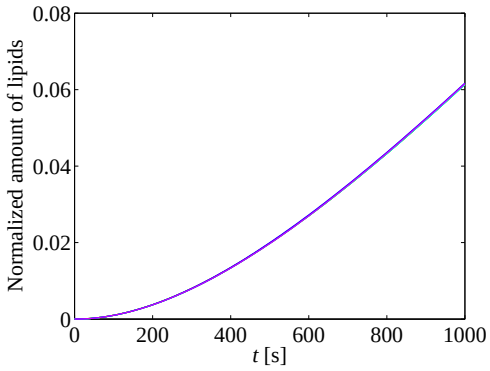

Figure 3.4: Integration of lipid concentration for the number of elements shown in Table 3.1 as a function of time. The ten curves overlap almost everywhere.

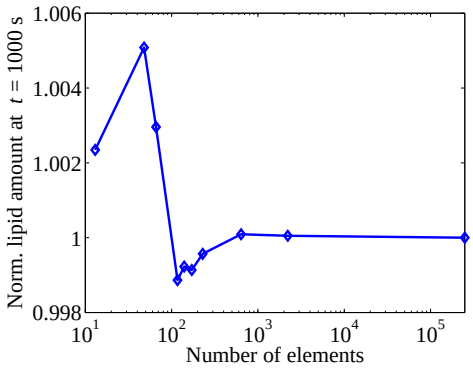

Figure 3.5: Integration of lipid concentration after 1000 seconds for the number of elements shown in Table 3.1.

graphs start close to zero. At this point, the differentiation and lipid production processes have only begun in the over refined mesh model, where nodes are close together in the cell layer, so that secreted factor can reach the cells again by diffusion. As time increase, all the models resemble the over refined mesh model, and goes towards unity. The same data is plotted in Fig. 3.7, where only deviations in the domain of ± 1 % are shown. It is clear that especially the three coarsest mesh models are imprecise, and should be avoided. It is confirmed that the *extremely fine* setting is a good compromise between precision and computation power.

Cell Péclet number

An important measure in the computational fluid dynamics is the *cell Péclet number*, which assures that the advection through an element is not dominated by diffusion. This is important for the numerical stabilization. The cell Péclet number is defined as [20]

$$Pe_{\mathrm{c}} = \frac{vh}{2D}, \tag{3.9}$$

where v is the velocity, h is the element size and D is the diffusion coefficient. Using the maximum velocity from Section 2.3, the maximum element size of $l_{\mathrm{rc}}/100$ and the diffusion coefficient of Eq. (3.2), the cell Péclet number in the center of the reaction chamber is $Pe_{\mathrm{c}} = 2.53$. However the velocity decrease along the domain boundaries, and the cell Péclet number is less than unity in some parts of the plane. Here, diffusion might cause instabilities. Thus the predefined velocity profile is not only a way to safe computation time, but also saves us from numerical instabilities.

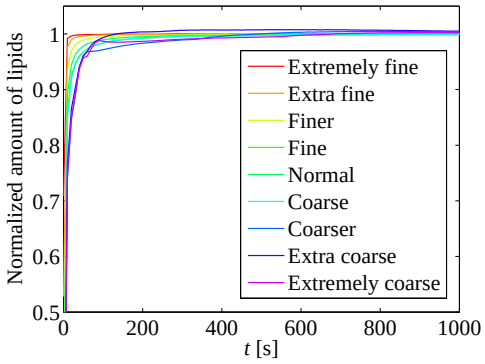

Figure 3.6: Lipid production vs. time, normalized with the over refined model.

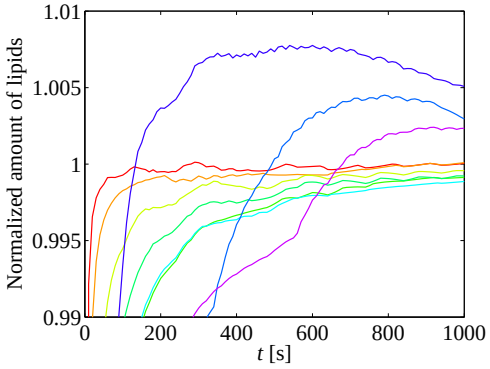

Figure 3.7: Zoom of Fig. 3.6, showing the difference in lipid production of different mesh parameters. Legends as in Fig. 3.6.

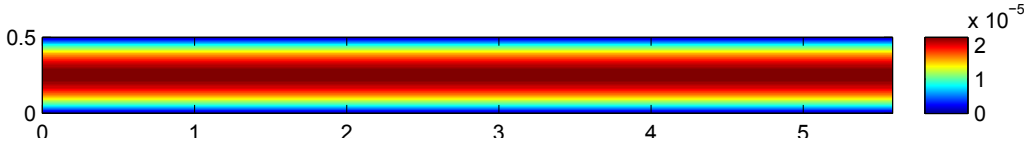

Figure 3.8: Velocity magnitude in the reaction chamber in m/s.

3.1.4 Verification of the idealized model

We will now go through the solution of the idealized model to verify that the processes in the system has happened as expected. The velocity field of the medium was derived in Section 2.3, and has therefore been defined as the pre-computed profile shown in Fig. 3.8. The velocity field follows a parabolic profile with the maximum velocity of $v_{\max} = 22$ µm/s found in Eq. (2.51).

Initially, there is no factor in the medium. Fig. 3.9 shows the factor concentration in the reaction chamber after 100 seconds, corresponding to approximately one fifth of the characteristic time of the system. Factor has been secreted from the cell layer on the bottom, and diffuse towards lower concentrations, in accordance with the diffusion equation. Moreover, the factor concentration is not symmetrical in the horizontal direction, or, to put it differently, the right half is not a mirror image of the left side. This phenomenon is caused by the advection term in the mass transfer equation. The interplay between diffusion and advection is very apparent because the two processes happen on the same timescale, namely that the factor diffusion coefficient is defined from the mean advection velocity in the reaction chamber. The factor concentration ranges from zero to approximately $f = 180$ mM. Thus, in the first phase of the experiment, concentrations lower than the threshold value of $f = 20$ mM are found close to the cells, and the differentiation of cells is limited by factor deficiency.

In the last time step of the simulation, $t = 1000$ s $\approx 2\tau$, most of the cells have differentiated. Thus the factor is being secreted with a constant rate from the cell layer, and none of the factor is absorbed for differentiation, Fig. 3.10. The situation resembles a steady-state solution. Factor concentrations of minimum $f_{\min} \approx 200$ mM are found along the cell layer, and undifferentiated cells can differentiate with maximum rate determined by the reaction rate constant k_{ud}. The characteristic time of factor diffusion was defined with the height of the chamber as the characteristic length scale, whereas the advection time was defined from the length scale l_{rc}. Thus the factor can never diffuse upstream, and factor concentration of practically zero is found in the upper left corner of Fig. 3.10.

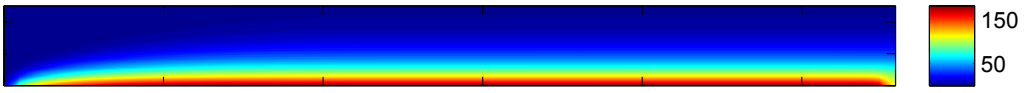

Figure 3.9: Factor concentration after $t \approx \tau/5$. The color bar has units of mM.

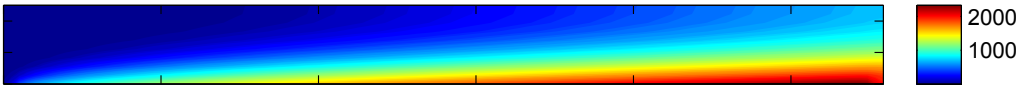

Figure 3.10: Factor concentration after $t \approx 2\tau$. The color bar has units of mM.

The concentrations of undifferentiated and differentiated cells are shown in Figs. 3.11 and 3.12, respectively. In both figures, the concentration has been normalized to the initial concentration of undifferentiated cells, u_0. Thus the initial concentrations of $u = u_0$ and $d = 0$ are represented as the dark blue straight lines at 1 and 0, respectively. At the last time step, $t = 1000$ s, 86 % of the cells have differentiated. Figs. 3.9 and 3.10 showed that there was a factor concentration higher than the threshold value, and the differentiation therefore happened with the maximum rate, $R_{\mathrm{ud,max}} \approx k_{\mathrm{u}} u$. The equation for the rate of change of concentration of undifferentiated cells in each point of the cell layer is then reduced to

$$\frac{\partial u}{\partial t} = -k_{\mathrm{u}} u, \tag{3.10}$$

an ordinary differential equation with the solution

$$u(t) = u_0 \left[1 - \exp\left(-k_{\mathrm{u}} t\right)\right]. \tag{3.11}$$

Diffusion of the cells has been ignored in Eqs. (3.10) and (3.11). However, since the factor concentration is above the threshold value along the cell layer, the conditions for cell differentiation is uniform, and diffusion does not contribute in this case. Thus the concentration of undifferentiated cells decays exponentially with time, and the difference in u between the two time steps decrease exponentially with time, and u approaches zero for infinite time. The opposite happens for the concentration of differentiated cells.

The exponential behavior is obvious in Fig. 3.13, where the total number of undifferentiated and differentiated cells in the cell layer has been found by integration and plotted

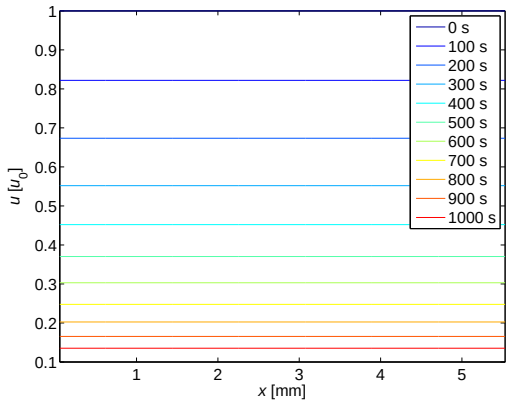

Figure 3.11: Concentration of undifferentiated cells along the cell layer at 11 selected time steps, normalized to the initial undifferentiated cell concentration u_0.

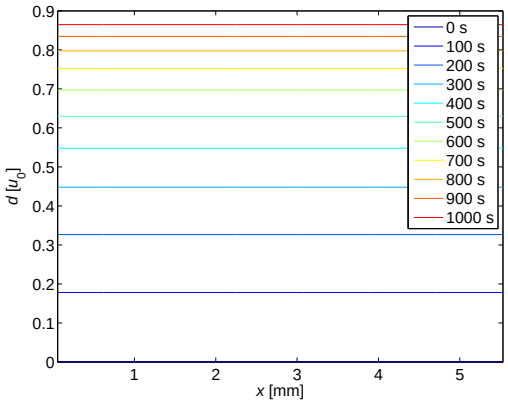

Figure 3.12: Concentration of differentiated cells along the cell layer at 11 selected time steps, normalized to the initial undifferentiated cell concentration u_0.

versus time. In addition, dotted lines show the number of cells at a constant differentiation rate of $R_{\mathrm{ud},0}k_{\mathrm{ud}}u_0$. The solid and the dotted lines overlap at small times, confirming that the differentiation clearly follows the estimated initial rate. Moreover, we see a direct measure of the characteristic time scale τ, where the dotted lines reach 0 and 1, respectively.

The lipid concentration is shown in Fig. 3.14. It resembles the concentration of differentiated cells in Fig. 3.12. Yet there is one major difference, namely that the rate of lipid production is low in the beginning, and increase as more cell have differentiated and initiated lipid production. Thus the rate is low in the beginning, and then approach a constant rate as most cell have differentiated.

The nutrition consumption was implemented by letting the flux of nutrition through the bottom boundary follow the rate of differentiation R_{ud}. The resultant concentration fields after $t = 100$ s and $t = 1000$ s are shown in Figs. 3.16 and 3.17, respectively. At the early stage, the differentiation rate is high, and the nutrition concentration close to the cell layer is 0.7 % lower than the background concentration. The 100 s correspond to only 1/5 of τ, the time it takes nutrition to diffuse from top to bottom of the reaction chamber. Therefore, a decrease in concentration is only observed in the lowest part of the chamber. At the late stage, Fig. 3.17, most of the cells have differentiated, and the differentiation rate is lower. One characteristic time scale has passed. The lowest concentration is found along the cell layer. It is 0.3 % lower than the background concentration. Less nutrition is now being consumed. As the nutrition now has had time to diffuse from top to bottom of the reaction chamber, a decrease in concentration is observed in the entire height of the chamber at the right outlet boundary.

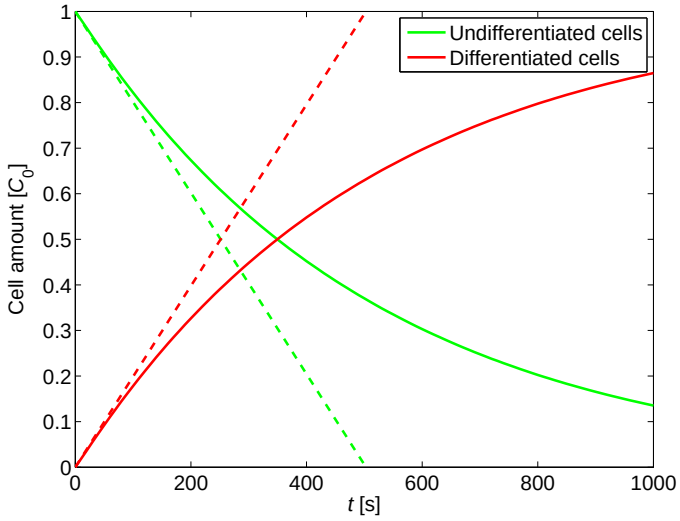

Figure 3.13: Differentiation of cells. The graphs show the integration of concentrations of undifferentiated and differentiated cells, respectively. The dashed lines show the expected cell amounts with constant maximum differentiation rate. All cell amounts have been normalized with the initial amount of undifferentiated cells.

The dynamics of the nutrition concentration are further investigated in Fig. 3.15, where the concentration field integrated over the entire domain N is plotted versus time. The graph is normalized with the background nutrition amount N_0. Thus the curve initiates at $N/N_0 = 1$ at time $t = 0$, where no differentiation has happened and no nutrition consumed. It then decreases due to the consumption. However, after approximately $t = 250$ s $\approx \tau/2$, the flux into the system from advection through the inlet boundary equalizes the flux out of the system from reactions on the cell layer boundary. After that, the inflow of new nutrition is larger than the consumption, and the curve increases, before approaching the background amount asymptotically.

To sum up the idealized model, the integration of all of the five independent variables are plotted on a logarithmic scale in Fig. 3.18. The green line depicts the variable U, the integration of the dependent variable u over the cell domain Ω times the width of the channel. U is the total number of undifferentiated cells in the system, mathematically defined as

$$U(t) \equiv w_{\mathrm{rc}} \int_{\Omega} u(x,t)\,\mathrm{d}x. \tag{3.12}$$

The integration of differentiated cell concentration and lipid concentration are performed similarly, while the amount of nutrition and factor are found by integration over the entire reaction chamber.

Recalling that the initial concentration of undifferentiated cell was set to $u_0 = 1$ m^{-1} and that the area of the cell layer is in the range of mm^2, the value of U is in the order of 10^{-6}. Thus the denomination 'number of cells' cannot be used directly for the idealized

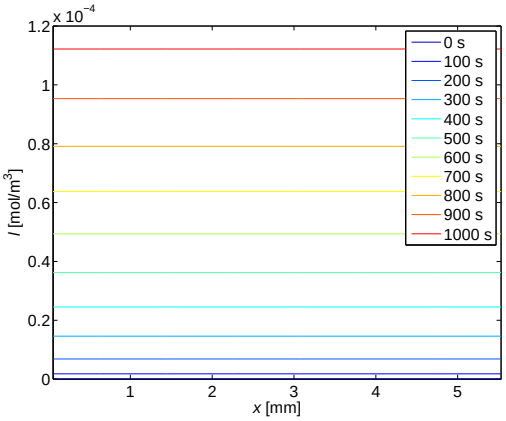

Figure 3.14: Concentration of lipids along the cell layer at 11 selected time steps.

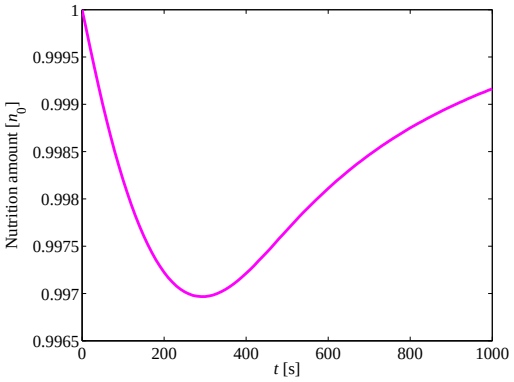

Figure 3.15: Integration of nutrition concentration versus time, normalized by the background concentration.

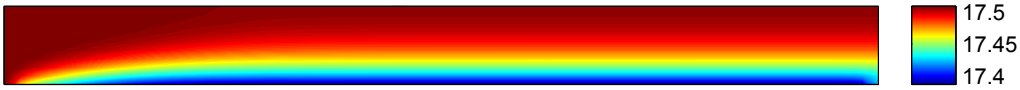

Figure 3.16: Nutrition concentration after $t \approx \tau/5$. The color bar has units of mM.

model. The number should be multiplied with the actual number of cells per square meter to make directly physical sense. However, the curve shows clearly how the number of undifferentiated cells decreased with a nearly exponential rate.

The opposite tendency is observed for the number of differentiated cells, showed by the red curve. The number of differentiated cells is derived equivalently to Eq. (3.12), and the sum of the green and red curves is constant the starting point of the green curve, namely the initial cell number U_0. Since we have ignored cell death, the sum of undifferentiated and differentiated cells in the system is constant. These curves correspond to those in Fig. 3.13.

As previously discussed, the increase in differentiated cell amount is faster than the lipid production initially. Later, the amount of lipids grow faster than the amount of differentiated cell lipids. This is obvious in the figure, where the blue lipid curve crosses the red curve representing differentiated cells after some time. The amount of lipids is the only quantity that has no steady-state equilibrium value.

The amount of factor is represented by a cyan curve in Fig. 3.18. Since the undiffer-

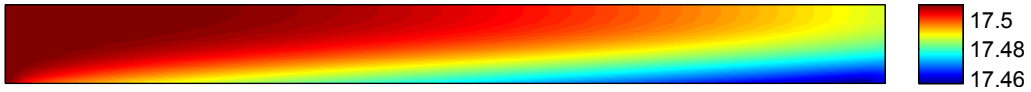

Figure 3.17: Nutrition concentration after $t \approx 2\tau$. The color bar has units of mM.

entiated and differentiated cells secrete factor with the same rate in the idealized model, ($k_u = k_d$), the total secretion is constant. Some of the factor substrate is absorbed for differentiation, but the overall amount is increasing throughout the studied time domain of $t = 1000$ s $\approx 2\tau$. As all of the cells have differentiated, the amount of factor reach an equilibrium where the secretion rate matches the flushing through the outlet.

The amount of nutrition was treated in Fig. 3.15. The same data is used for the pink line in Fig. 3.18, but the valley cannot be detected with this range of the y-axis, so it resembles a straight line.

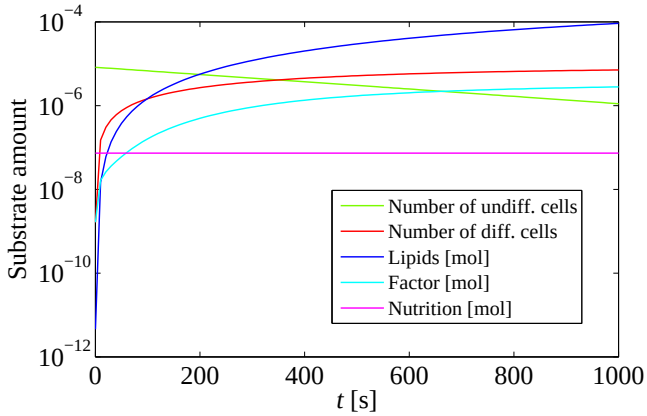

Figure 3.18: Integration of all dependent variables.

We have seen how the idealized model agrees with our expectations for all of the variables. Moreover, the characteristic time τ appears several times as an important factor of the system. The model can successfully be solved in seconds on an ordinary pc.

The parameters were determined in order to obtain interplay between the processes of advection, diffusion and reaction, i.e. to have characteristic time scales around τ. Therefore, some elements of the idealized model are orders of magnitudes different from reality. In the following section, we will attempt to set up a more realistic model.

3.2 Realistic model

More realistic parameter values are here estimated or presented, and implemented to the idealized model. Thus the model is tuned to give results that might be quantitatively comparable to the experiments.

3.2.1 Diffusion coefficients

Experiments with cell tracking every hour have been conducted, and it has been observed that cells tend to move around on the surface with a few cell diameters between each logging. Thus the distance between the position of a given cell, or fat colony, at time

zero and after one hour is estimated to be in the order of $s = 100$ μm. The cell has been moving by a random walk-like behavior, and we can estimate the diffusion coefficient for diffusion of stem cells on a two dimensional surface to be [17]

$$D_{\mathrm{c}} = \frac{s^2}{4t}. \tag{3.13}$$

The value of $D_{\mathrm{c}} = 2.50 \times 10^3$ μm^2/h $= 6.94 \times 10^{-13}$ m$^2/s$ corresponds well to the literature, where e.g. *Gail and Boone* [21] has estimated the diffusion coefficient of mouse fibroblasts to be one third of our estimate, namely $D_{\mathrm{c}} = 858$ μm^2/h $= 2.38 \times 10^{-13}$ m$^2/s$. The estimate of a cell moving 100 μm/h is a rough estimate, so the value from *Gail and Boone* will be used in the model for undifferentiated and differentiated cells. The lipid vacuoles grow inside the cell membrane, and the same diffusion coefficient is therefore used for the lipids.

The factor substrate is suspected to be a type of cytokine. *DiLeo et al.* estimate the diffusion coefficient of three different cytokines by a mathematical model compared to experimental results [22]. One of the cytokines is the Interleukin-6 (IL-6), a protein that in humans is encoded by the IL6 gene [23]. Though their estimate is based on diffusion in microporous beads, we will use the same value for our factor diffusion in the medium. The value is $D_{\text{il-6}} = 8.49 \times 10^{-12}$ m^2/s, corresponding to 1/30 times the value used in the idealized model.

3.2.2 Reaction rate constants

Dependent on the conditions, the first vacuoles have appeared in the reaction chamber after three or four days. At first we found it plausible that the differentiation of cells form a positive feedback loop, so that differentiation of cells stimulates the differentiation of nearby cells. Thus it would take some time to attain a critical amount of differentiated cells, before the rate of differentiation is significant, and the lipid production can speed up. The feedback loop has been explained by assuming that differentiated cells secrete significantly larger quantities of factor than the undifferentiated cells [24].

In the realistic model introduced in this chapter, this distinction would be implemented as a larger metabolic rate of the undifferentiated cells or, equivalently, $k_d > k_u$.

However, this explanation has recently been challenged. Consider Fig. 3.19, where the progress of an experiment is shown by measuring intercellular distances over time. The red graph shows the distribution of nearest neighbor distance of undifferentiated cells at day one.

The bars of Fig. 3.19(a) indicate the first observed vacuole clusters in the experiment. It shows that 6 differentiated cells have been detected for the first time in this time step. The distances between these and the nearest differentiated cell from an earlier time step seem to be stochastic distributed within a few hundred on microns. Thus there is no evidence that differentiated cells secrete significantly larger amounts of factor, since that would cause cells in the proximity of differentiated cells to experience higher concentrations of factor, and hence commence the differentiation process earlier.

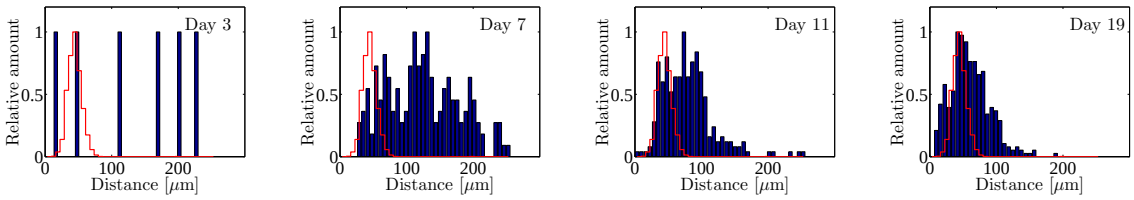

(a) (b) (c) (d)

Figure 3.19: Distance to neighboring cells and newly differentiated cells over time. The blue bars indicate distances from newly differentiated cells to nearest differentiated cell after 3 (a), 7 (b), 11 (c) and 15 days (d). The red graph shows the distribution of distance between nearest neighbors of undifferentiated cells. All data has been normalized by the largest value of each data set. Data processing by Søren Vedel [12].

This conclusion is supported by Fig. 3.19(b), where the corresponding number of newly differentiated cells at day seven are shown. The distribution is wide and displaced towards larger distances between existing and newly differentiated cells in comparison to the standard intercellular distance shown by the red graph. As the newly differentiated cells are not necessarily the nearest neighbor of existing differentiated cells, the differentiation process does not seem to be attracted to the areas close to already differentiated cells. Thus we do not have indications of difference in the factor secretion rates of undifferentiated and differentiated cells.

In Fig. 3.19(c), a substantial part of the cells are differentiated, and the distance from any arbitrary point to a differentiated cell is close to the nearest neighbor distance of Eq. (3.16). Therefore, the variance of the distance between existing and newly differentiated cells decreases. This effect is enhanced in Fig. 3.19(d), where the last available data set is presented. After 19 days, many cells have differentiated, and the bars resemble the nearest neighbor distribution.

Having established that the rate of secretion of factor is similar for undifferentiated and differentiated cells, we will use the condition of

$$k_u = k_d \tag{3.14}$$

in the following computations.

To find out if the average distance between nearest neighbors agree with our expectations, consider Fig. 3.20. By counting the number of cells in a confined area of the chamber bottom, the density of cells has been estimated to be $u_0 = 898$ mm^{-2} for the relevant conditions [2]. A relation between cell density and average distance between nearest neighbors is estimated by assuming that the cells are arranged in a periodic lattice, where each cell has six equally distant nearest neighbors. The geometry is shown in Fig. 3.20. The dark rectangle in the figure defines a unit cell of the lattice, and the covered cell

fractions sum into $n = 2$ whole cells. The angles of the triangles formed by the cells all have angles of $\theta = \pi/3$. The area of the unit cell can then be found from trigonometric considerations to be

$$A_{\mathrm{u}} = \sqrt{3}h^2 \tag{3.15}$$

where h is the distance between neighboring cells. The expected average distance between nearest neighbors is then

$$h_{\mathrm{ave}} = 3^{1/4}\sqrt{\frac{n}{u_0}} \approx 62 \text{ µm}. \tag{3.16}$$

This value corresponds well with the mean distance in Fig. 3.19, thus the assumption of a uniform cell distribution yields consistent average distance between nearest neighbors with the experimental result, though the data shows a variance around this point. The expected distance between nearest neighbors is marked by a dotted line in Fig. 3.19.

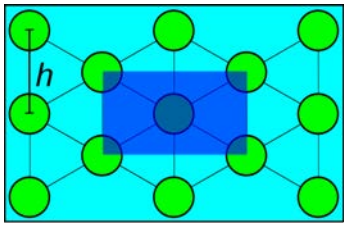

Figure 3.20: Sketch of the cells in the reaction chamber. The green circles mark the positions of undifferentiated cells under the assumption an equally spaced distribution with a distance of h between neighboring cells. The blue rectangle defines a unit cell of the lattice. Dimensions not to scale.

Now, having established that the two secretion rate constants k_{u} and k_{d} are equal, the value should be determined. We know from experiments that the vacuoles appear on the reaction chamber bottom after typically 3 days. Since we do not know the identity of the factor substrate and the reactions of factor secretion, differentiation and lipid production, the rate constants from the idealized model are scaled to give the differentiation time observed in the experiments. The differentiation took place within a time of approximately 2τ, at it should be scaled to 3 days $\approx 10^5$ s. Therefore, the reaction rate constants are multiplied by a factor of

$$\frac{Q\,(60 \cdot 60 \cdot 24 \cdot 3 \text{ s})}{2l_{\mathrm{rc}}w_{\mathrm{rc}}h_{\mathrm{rc}}} = 3.88 \times 10^{-3}, \tag{3.17}$$

yielding the more realistic rate constants of Table 3.2.

3.2.3 Lipid production

An estimate of the lipid production is obtained from a scan of the bottom of the reaction chamber. Fig. 3.21 shows a part of the result of an experiment where a medium including the adipogenic growth factors has been infused to the cells, after 20 days. The white

Table 3.2: Values of parameters used in the realistic model and the values relative to the idealized model.

Parameter	Symbol	Value	Rel. value
Undif. cell secretion rate const.	k_{u}	7.72×10^{-6} s^{-1}	3.88×10^{-3}
Dif. cell secretion rate const.	k_{d}	7.72×10^{-6} s^{-1}	3.88×10^{-3}
Differentiation rate constant	k_{ud}	3.86×10^{-7} m^3/(mol $\cdot$ s)	3.88×10^{-3}
Lipid production rate constant	k_{l}	7.72×10^{-6} s^{-1}	3.88×10^{-3}
Undif. cell diffusion coefficient	D_{n}	2.38×10^{-13} m^2/s	7.68×10^{-6}
Dif. cell diffusion coefficient	D_{n}	2.38×10^{-13} m^2/s	7.68×10^{-6}
Factor diffusion coefficient	D_{n}	4.69×10^{-12} m^2/s	3.41×10^{-2}
Nutrition diffusion coefficient	D_{n}	6.00×10^{-10} m^2/s	2.41
Lipid diffusion coefficient	D_{n}	2.38×10^{-13} m^2/s	7.68×10^{-6}
Initial cell density	u_0	8.98×10^{8} m^2/s	8.98×10^{8}
Nutrition cons. per reaction	α	2.87×10^{-11} m^2/s	2.87×10^{-7}

circular formations are vacuoles produced by differentiated cells. Converting the image to grayscale, we can compute the area covered by vacuoles. The approach depends on the threshold value, which determines whether a pixel shows lipids or not. A good threshold value has proven to be 0.7, so that each pixel with a larger greyscale value depicts lipid. The result of the image analysis is shown in Fig. 3.22, and comparing it to Fig. 3.21 documents that most vacuoles are being counted. The lipid filled area is plotted as a function of the threshold value in Fig. 3.23. It shows that if the threshold value is very low, all pixels are counted as lipid covered, and the area of lipids is equal to the entire domain considered. Similarly, if the threshold value is too high, no vacuoles are detected. The applied value is marked by a red circle, corresponding to a coverage of $\sigma = 11.4$ % of the chamber bottom. The scale bar in Fig. 3.21 indicates a distance of 50 μm, and from that we can estimate a typical vacuole radius of $r_{\mathrm{v}} = 5$ μm. Assuming that the shape of the vacuoles are half spheres, the volume of one vacuole is

$$v_{\mathrm{v}} = \frac{2}{3}\pi r_{\mathrm{v}}^3. \tag{3.18}$$

The total number of vacuoles in a reaction chamber is

$$N_{\mathrm{v}} = \frac{l_{\mathrm{rc}} w_{\mathrm{rc}} \sigma}{\pi r_{\mathrm{v}}^2}, \tag{3.19}$$

and the total volume of lipids can now be determined as

$$V_{\mathrm{l}} = \frac{2}{3} r_{\mathrm{v}} l_{\mathrm{rc}} w_{\mathrm{rc}} \sigma. \tag{3.20}$$

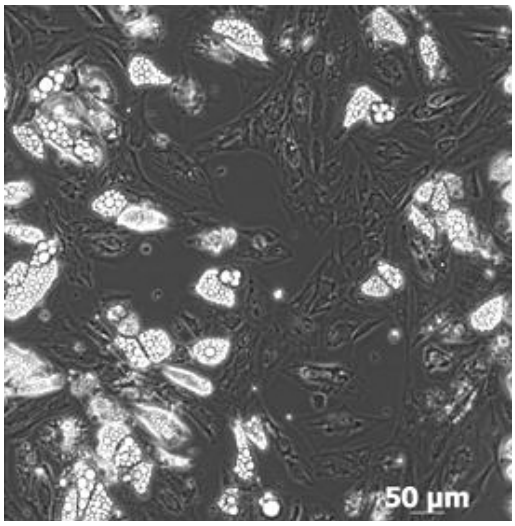

Figure 3.21: Original scan of vacuoles from a typical experiment. Image from *Hemmingsen*[2].

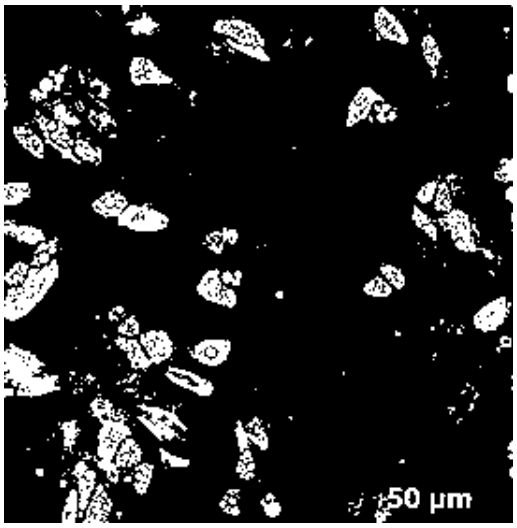

Figure 3.22: Definition of area occupied by vacuoles.

Thus assuming that the selection shown in Fig. 3.21 is representative for the entire reaction chamber, though it only represents around 5%, it is estimated from Eqs. (3.18) and (3.20) that the number of vacuoles in the system is $N_\mathrm{v} \approx 10^4$, yielding a total volume of $V_\mathrm{l} = 3.2$ nL.
A more thorough image analysis is carried out by *Vedel*[12].

The relation between the amount of nutrition consumed for lipid production and the nutrition infused through the medium can be estimated from calorimetric considerations [25]berg2002. The amounts of energy required to deposit 1 kJ of fat in rats has been shown by regression analysis to be 1.36 kJ [26]. However, the conversion from sugars to fat on the microscopic scale of the individual cells is almost lossless. Thus the percentage of converted nutrition to infused nutrition can be estimated. The mass of glucose energy equivalent to the fat stored in the system is

$$m_\mathrm{g,con} = \frac{V_l \rho_l \varphi_l}{\varphi_g}, \tag{3.21}$$

where $\rho_l = 0.9196$ g/mL and $\varphi_\mathrm{l} = 9.505$ Cal/g $\approx 3.98 \times 10^7$ J/kg is the mass density and energy density of adipose tissue, respectively [27, 28], and $\varphi_g = 16$ kJ/g $= 1.6 \times 10^7$ J/kg is the energy density of glucose [29]. Thus 7.3 µg of nutrition has been deposited as vacuoles on the chamber bottom.
The amount of glucose infused to the system over a period of $\Delta\tau$ is

$$m_\mathrm{g,inf} = QMn_0\Delta t \tag{3.22}$$

where $M = 180.16$ g/mol is the molar mass and $n_0 = 17.51$ mM is the stated concentration of glucose in the medium [11]. The experiment shown in Fig. 3.21 has been running for

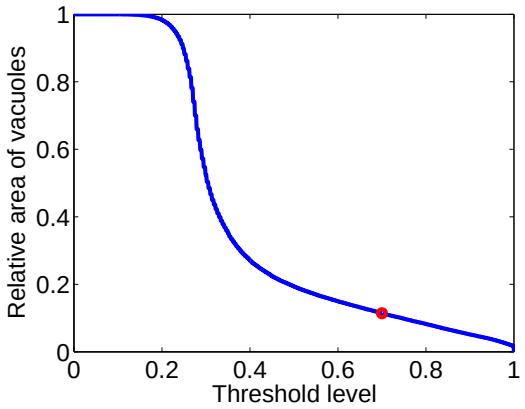

Figure 3.23: The area occupied by lipids decrease for larger levels of the grayscale threshold value. The red circle marks the applied value and the corresponding relative area.

20 days, so the total amount of infused glucose is $m_{\mathrm{g,inf}} = 45$ mg. The percentage of converted nutrition is then

$$\frac{m_{\mathrm{g,con}}}{m_{\mathrm{g,inf}}} = 0.016\ \%. \tag{3.23}$$

It was shown in Section 2.2 that the diffusion time of dextrose is comparable to the advection time. Thus the Péclet number is around unity, and a substantial fraction of the dextrose has time to reach the cells by diffusion. We can therefore conclude that there is be a surplus of dextrose, and we can safely replace the factor of $\tanh(n/n_{\mathrm{t,ud}})$ by 1 in Eq. (2.59), Eq. (2.62) and Eq. (2.64).

In the model, the nutrition consumption is implemented as a flux of nutrition per stem cell differentiation, and not from the lipid production. However, we will use the result of Eq. (3.23) to estimate the amount of nutrition used in the differentiation of one cell. The realistic model will be solve for time steps up to $t_{\max} = 3$ days. Thus the total number of infused nutrition is $Qn_0t_{\max}$, and the number of cell differentiations is approximately the initial concentration of cells times the area of the reaction chamber. We then get

$$\alpha = 0.016\ \frac{Qn_0t_{\max}}{u_0 l_{\mathrm{rc}} w_{\mathrm{rc}}} = 8.0 \times 10^{-13}\ \mathrm{mol}. \tag{3.24}$$

3.2.4 Numerical Analysis of the Realistic Model

Figure 3.24: Factor concentration after $t = 0.3$ days in the realistic model. The color bar has units of mM.

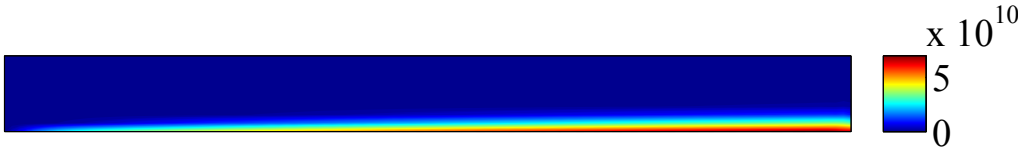

Figure 3.25: Factor concentration after $t = 3$ days in the realistic model. The color bar has units of mM.

The parameters have now been scaled to more realistic values. The real flowfield was used in both the idealized and the realistic models. Thus the characteristic advection time is the same, while e.g. the characteristic time for diffusion of cells has changed. The model is now solved for the three days it usually takes to develop lipid vacuoles in the laboratory. Therefore, the results will differ from the idealized model. The cell diffusion time is now one tenth of the last time step, where the advection time is one thousandth. The factor diffusion coefficient D_f was also changed, so the differentiation process now requires higher factor concentrations, because a large part of the factor is flushed out instead of being absorbed by the undifferentiated cells.

The factor concentration is shown in Figs. 3.24 and 3.25. After 0.3 days, there is much more factor than in the idealized model. At the same time, the factor concentration is only high along the cell layer, because all solutes are flushed out before they have moved towards the center of the reaction chamber by diffusion. This picture is more apparent after 3 days in Fig. 3.25.

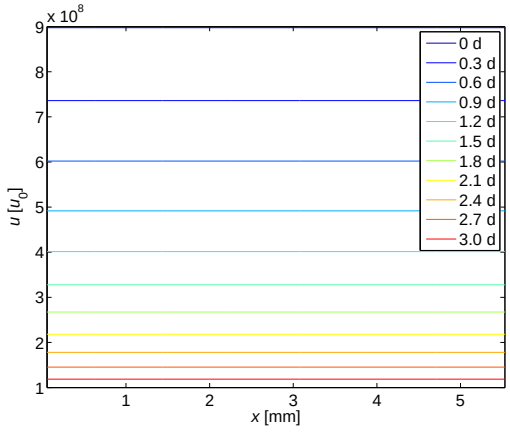

Figure 3.26: Concentration of undifferentiated cells along the cell layer at 11 selected time steps in the realistic model, normalized to the initial undifferentiated cell concentration u_0.

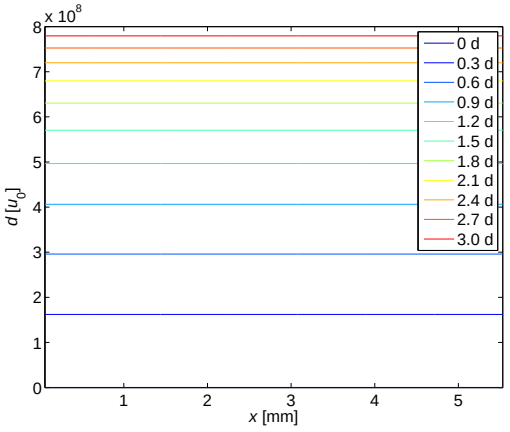

Figure 3.27: Concentration of differentiated cells along the cell layer at 11 selected time steps in the realistic model, normalized to the initial undifferentiated cell concentration u_0.

The reaction rate constant of differentiated has been scaled so that the differentiation process has almost finished after 3 days. Therefore, the concentrations of undifferentiated and differentiated cells shown in Figs. 3.26 and 3.27 resembles the corresponding figures from the idealized model, Figs. 3.11 and 3.12, though the time scale is different.

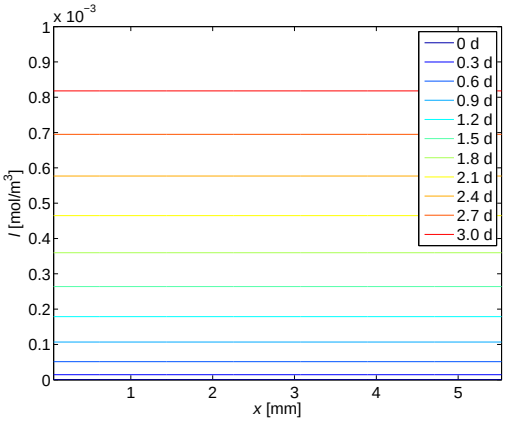

Figure 3.28: Concentration of lipids along the cell layer at 11 selected time steps in the realistic model.

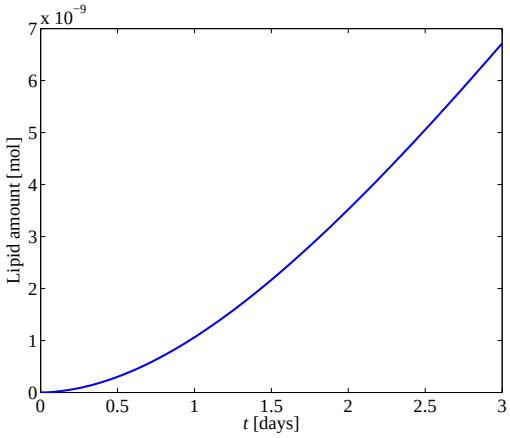

Figure 3.29: Integration of lipids in the realistic model.

As observed in experiments, most cells have differentiated and started lipid production after the first few days. This time scale is an important timescale in the realistic model. The lipid concentration along the cell layer is shown in Fig. 3.28. The curves lie close for early time steps. As most of the cells have differentiated at the last time steps, the lipid production is more constant, and the distance between two neighboring curves in Fig. 3.28 gets more constant. This is supported by Fig. 3.29, where the total amount of lipid in the reaction chamber is plotted against time. The curve resembles an exponential growth initially, but then stabilize at a constant production rate indicated by the straight line in the last part of the graph. The nutrition consumption was estimated to be 0.016 % of

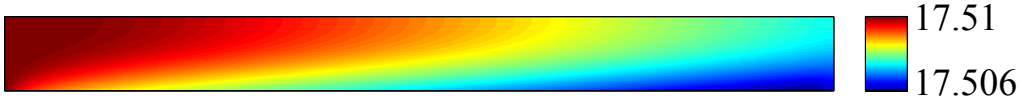

Figure 3.30: Nutrition concentration after $t = 0.3$ days in the realistic model. The color bar has units of mM.

the infused nutrition. This fits well with Fig. 3.30, where the nutrition concentration in the reaction chamber after 0.3 days is plotted.

The total amount of all substances in the system at the last time step is shown in

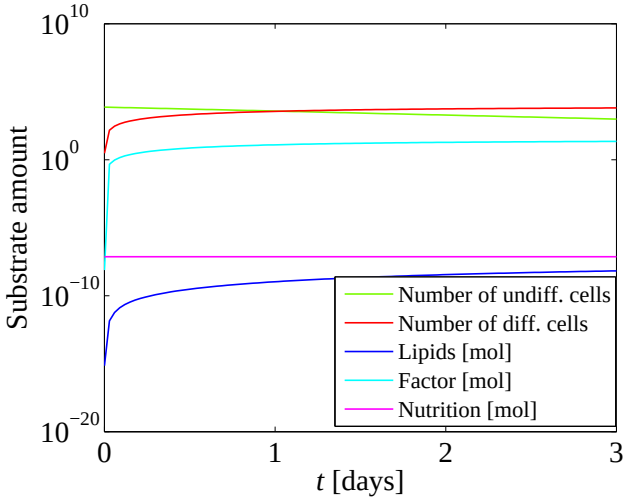

Figure 3.31: Integration of all dependent variables in the realistic model.

Fig. 3.31. The overview shares several dynamics with the corresponding Fig. 3.18 from the idealized model. The number of cells is larger, a constant of nearly 7000 cells in total. The half-life period is around 1 day, again approximately one third of the total time.

The amount of factor is much larger than in the idealized model. The lipid production rate constant k_l was scaled with the new characteristic time of the system, but as the real initial cell concentration has been used so much more cells have been producing. Therefore the factor concentration end up around $f = 10^7$ M, where a typical concentration of cytokines is in the order of nanomolar of even picomolar. The magnitude of the factor concentration field should be changed be scaling the values of k_u, k_d, k_ud and β to be directly comparable to experiments. However, since the identity of factor is still unknown, we cannot measure the concentration experimentally.

Chapter 4

Comparing the Model to Experiments

We will now apply the models to different phenomena that have been observed in the laboratory.

4.1 Flowrate dependence

It was shown in Section 2.2 that the available amounts of nutrition, differentiation factors etc. are not decreased at large flowrates. However, experiments have shown that flowrate is an important parameter for the rate of differentiation.

Fig. 4.1 shows three different reaction chamber bottoms in an experiment. The flowrates through each of these chambers are 33nL/min, 125nL/min and 500nL/min, respectively. All other conditions are the same for the three chambers. It is obvious that most fat has been produced in the one in the center. The increase in lipids from (a) to (b) probably has to do with the amount of differentiation factors etc. available. It has been found that a threshold flowrate is necessary to induce the differentiation. However, the low differentiation rate in Fig. 4.1 (c) cannot be explained from starvation. *Skafte-Pedersen* [7] has investigated if is could be caused by the high shear stress that follows from a high flowrate, but concluded that the adipogenic stem cells are not significantly affected by this.

Instead, we want to investigate if the low differentiation at high flowrate can be explained by flushing of the factor.

At high flowrates, more of the factor will move through the outlet by advection than at low flowrates. The investigations have been performed with the idealized, easy solvable model from Section 3.1, because the realistic model tend to break down with the very large flowrates we will implement.

At flowrates of the same order of magnitude as the real flowrate of $Q = 500\text{nL/min}$, the rate of differentiation is almost invariant. However, when the flowrate is increased by orders of magnitude, a change in differentiation rate is observed. The amount of undifferentiated and differentiated cells is plotted against time in Fig. 4.2 for 4 different

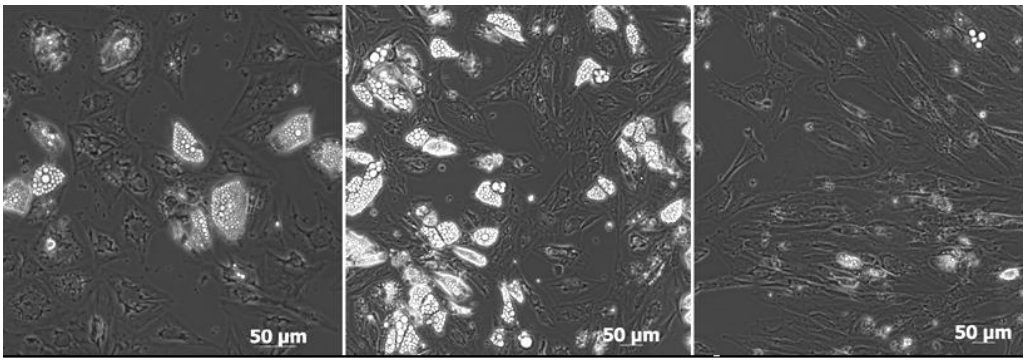

Figure 4.1: Effect of perfusion flowrate on the differentiation efficiency. Imaging of a representative experiment at day 20 after start of differentiation with flowrates of 33nL/min, 125nL/min and 500nL/min.

flowrates. The cyan curves represent the differentiation with the usual flowrate Q. They cross each other after $T_{1/2} = 349$ s in the idealized model, where half of the cells have differentiated.

They nearly overlap with the magenta curves, where the flowrate has been increased by a factor ten. The magenta curves cross at $t = 355$s, so the time it takes half of the cells to differentiate is extended with 2 %.

The effect is apparent when the flow rate is 100 times the normal flowrate, shown with green curves, and more obvious for 1000 times the normal flowrate (blue curves). The half-life is $T_{1/2} = 962$ s, an increase of 176 % from the standard conditions.

Flowrates of 1000 times the normal are not possible to obtain in a standard laboratory. However, the model is an idealization, an the absolute values of the parameters cannot be directly compared to the experiments. Rather, the investigation demonstrate that it is possible to reduce the differentiation process by flushing the factor out of the system. If the experimental setup can be translated to the domain of the last curves in Fig. 4.2, the flowrate can cause a decrease in differentiation.

4.2 Cell concentration dependence

Assuming that a secreted factor is an essential element in the stem cell differentiated, it has been discussed whether a uniform or a spatially increasing differentiation rate along the flow direction should be expected. The initial cell distribution in the experiments has been investigated by *Hemmingsen* [2], and with the newest pumping systems, no difference in cell density has been detected between the inlet and outlet end of the reaction chamber. As a consequence, the rate of factor secretion is assumed to be uniform along the flowrate. That would mean that cells downstream experience larger factor concentrations than cells upstream, because factor is moved from upstream to downstream cells by advection. Following the assumptions in the models presented in Chapter 3, this would mean that the cells downstream initiate the differentiated process earlier than cells downstream. The

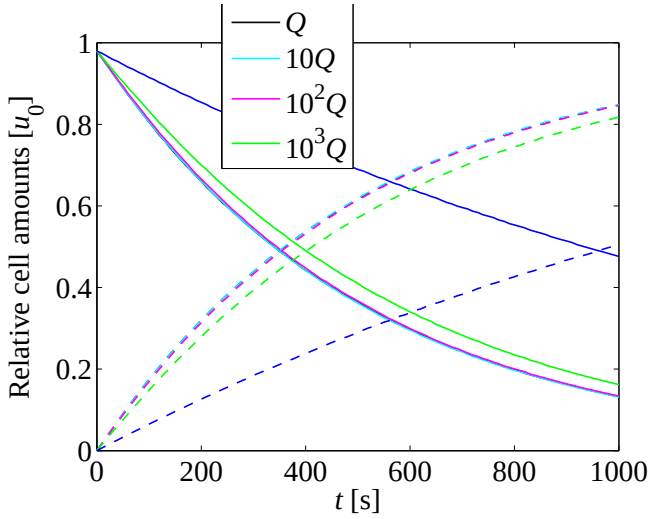

Figure 4.2: Differentiation of cells at 5 different flowrates. The solid lines are the integration of undifferentiated cells over the cell layer, normalized to the initial amount, and the dashed lines show the corresponding amount of undifferentiated cells.

lipid concentration along the reaction chamber at a given time would then be increasing from inlet to outlet, i.e. along the x-axis.

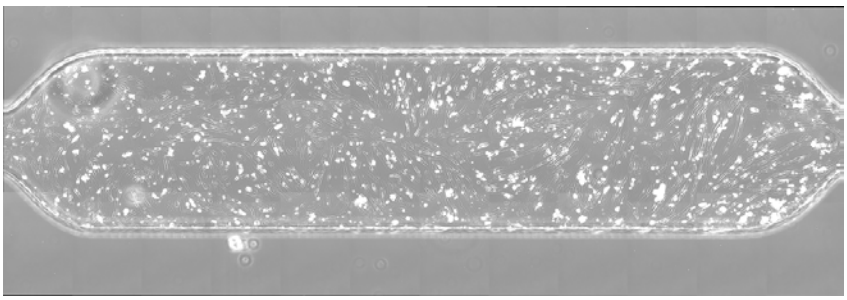

Figure 4.3: Scan of reaction chamber in an experiment. From file *20111127_Density gradient_500nL_Day19_Pos6.tif*.

However, the experiments have not indicated that more vacuoles are being produced downstream than upstream. A scan of a typical experiment is shown in Fig. 4.3. The figure include the entire expansion of the microchannel. Only the rectangle has been defined as the reaction chamber in the models.

The mean intensity of each column of pixels is plotted in Fig. 4.4. Thus the values is the average of each vertical line of Fig. 4.3. The green background marks the definition of the reaction chamber. We see that the mean intensity, a measure of the lipid concentration, is

almost constant from inlet to outlet of the reaction chamber. In Fig. 4.5, the concentration

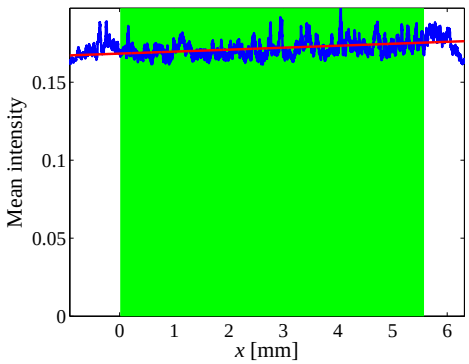

Figure 4.4: Distribution of vacuoles in the reaction chamber and linear trend line. The green area marks the reaction chamber.

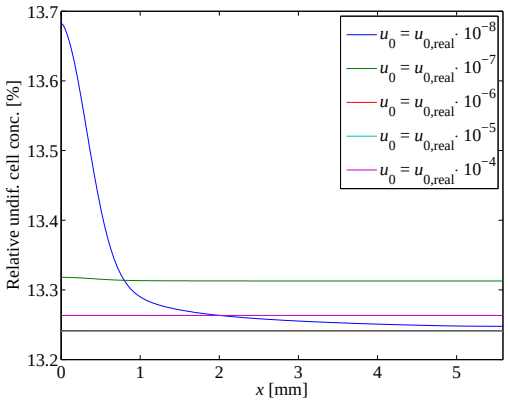

Figure 4.5: Concentration of undifferentiated cells for a range of initial concentrations after 3 days, normalized to the initial undifferentiated cell concentration u_0.

of undifferentiated cells along the cell layer after 3 days is plotted. The concentrations has been found by dividing the real initial cell concentration by 10^8, 10^7, 10^6, 10^5 and 10^4, respectively, in the realistic model. The concentrations have been normalized with the initial cell concentration of each simulation to make them comparable.

Equal for them all is the percentage of cell that still haven not differentiated after the three days, around 13 %. Yet a qualitatively difference is observed for the two curves with lowest initial cell concentrations, the blue and green curves. Here, the final concentration of undifferentiated cells is larger close to the inlet than close to the outlet. Thus at very low cell seeding densities, the cells downstream differentiate faster, because they can absorb secreted factor from cells upstream. For the all other values of initial cell concentration, there is no such difference along the x-direction of the reaction chamber. Simulations with initial cell concentrations around the real cell density in the experiments show the same behavior, and gives straight line and overlap with this group.

Thus we conclude that the behavior of an uneven differentiation due to advection of the factor is possible for extremely low cell seeding concentration. However, in the range of cell seeding densities applied in the lab, there is no such effect. The small slanting of the trend line in Fig. 4.4 may instead be caused by an uneven loading of the cells, where more cells have sediment in one end than in the other.

4.3 Dilution of differentiation factors

Dilution of the differentiation cocktail has proved to give higher vacuole production. An example is shown in Figs. 4.6 and 4.7, where an experiment is presented. The first shows

a scan of the reaction chamber bottom after 22 days, where a standard medium solution mixed with conditioned medium has been infused to cells with a seeding density of 900mm^{-}2. In the second, the adipogenic medium has been diluted to one fourth of the original concentration before mixing with conditioned medium. All other conditions are identical in the two experiments. It is obvious that the vacuoles in Fig. 4.7 are larger and closer to each other than in Fig. 4.6. We know that the adipogenic differentiation factors are essential for cell differentiation, but it appears that too high concentrations can inhibit the differentiation process. We want to apply the idealized model to this case, to investigate if toxicity can explain the decrease in differentiation at high differentiation factor concentration.

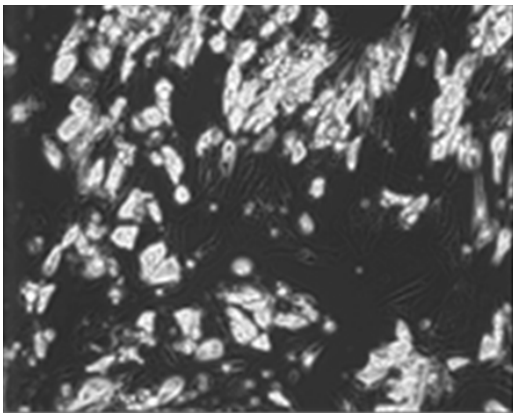

Figure 4.6: Scan of reaction chamber where the adipogenic cocktail has been mixed with conditioned medium.

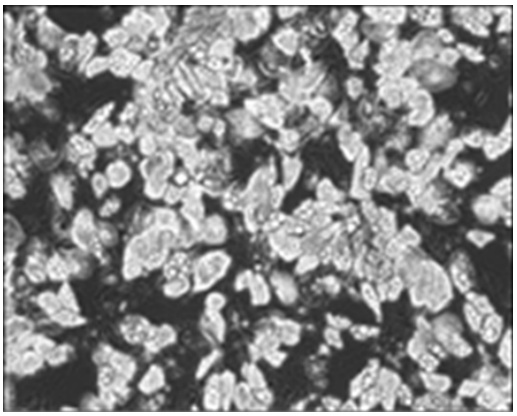

Figure 4.7: Scan of reaction chamber where the adipogenic cocktail has been diluted before mixing with conditioned medium.

The rate of differentiation is therefore defined to depend on the local concentration of differentiation factors, along with the concentrations of undifferentiated cells and factor. It is implemented by the variable n, which as usual covers nutrition, differentiation factors and other constituents of the medium. As usual, the mix will be referred to as nutrition. The differentiation rate is thus defined as

$$R_{\text{ud}} = k_{\text{ud}} u f_0 \tanh\left(\frac{f}{f_0}\right)\left[\tanh\left(\frac{n}{n_0/2}\right) - \tanh\left(\frac{n}{n_0}\right)\right], \tag{4.1}$$

where n_0 is the concentration of nutrition in the medium. The expression in the square bracket is the contribution from the nutrition dependence, and the rest is the rate used in the previous models. The nutrition contribution is composed of two terms. The first assures that the differentiation rate is low for $n < n_0/2$, and the second assures that the differentiation is low for $n > n_0$. The nutrition dependence contribution is plotted in Fig. 4.8. The differentiation rate R_{ud} is thus linear in n for small n, and peaks around

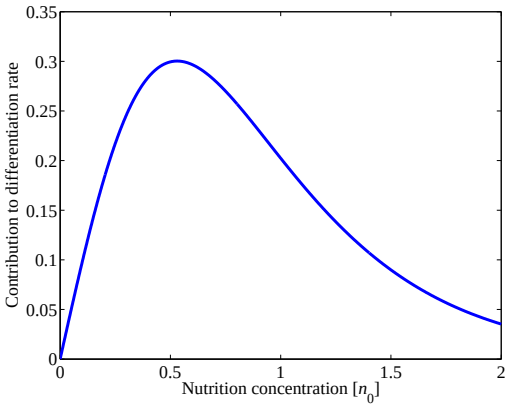

Figure 4.8: Nutrition dependence contribution to the differentiation rate.

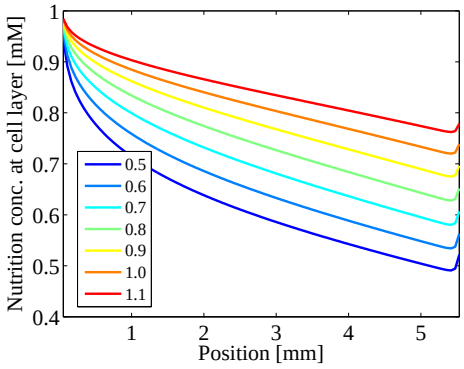

Figure 4.9: Final nutrition concentration along cell layer. The legends denote the background nutrition concentration compared to n_0.

$n = n_0$, before decreasing for large nutrition concentrations. We do not know which constituent of the medium that causes the differentiation inhibition. Thus the consumed amount of the toxic solute is unknown. In order to be able to enhance the dynamics of the applied differentiation nutrition dependence, we will assume that a substantial part of the solute is being consumed. Therefore, the amount consumed for differentiation of one cell is assigned the value of $\alpha = 0.01$ mol, a hundred times that used in the previous models. Since the toxic solute is unknown, the diffusion coefficient of glucose will be applied.

The nutrition concentration along the cell after $t \approx 2\tau$ layer is shown in Fig. 4.9. The value of n_0 in Eq. (4.1) is the same for all of the curves, while the nutrition concentration in the medium equals n_0 times the factor in the legends. In all cases, the nutrition concentration at the left end of the cell layer is equal to the background concentration, to which the concentration has been normalized. Thus all the curves start at unity, and decrease along the cell layer, where the nutrition is being consumed. The blue curves correspond to the smallest background nutrition concentration, where the background concentration fits the peak in Fig. 4.8. Thus the differentiation rate is large, and much nutrition is consumed. However, the total differentiation is larger for a background concentration of $0.8n_0$, depicted by the green line. This is obvious from Fig. 4.10, where the concentration of undifferentiated cells after $t = 2\tau$ is shown. We observed that green curve in Fig. 4.9 runs between 0.6 and 1. By integration, we find the average nutrition concentration af this case to be $n_{\text{ave}} = 0.75n_0$. Multiplying this concentration with the factor of 0.8 used for the background concentration, we get the actual nutrition concentration to be $0.6n_0$, which correspond well to the peak of Fig. 4.8. Therefore, we have the highest rate of differentiation in this case, which is evident from Fig. 4.10, where the green curve is the lowest, meaning that most cells have differentiated for this background concentration.

Another feature of Fig. 4.10 is the slope of the curves. The blue curves show a con-

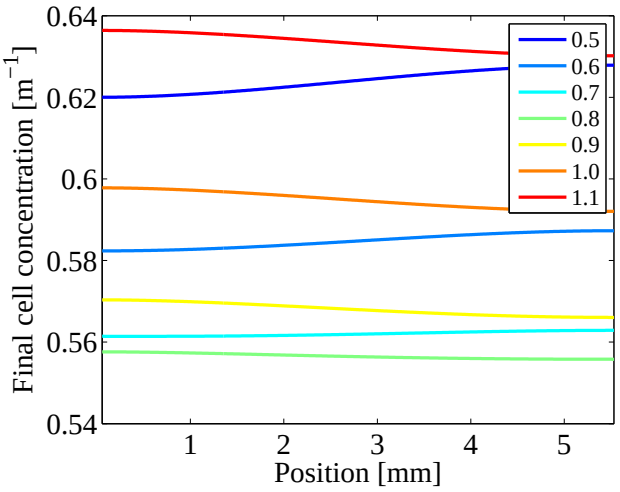

Figure 4.10: Undifferentiated cell concentration after $t \approx 2\tau$ for different nutrition concentration in medium. The legends denote the background nutrition concentration compared to n_0.

centration of undifferentiated cells lowest for small values of x, i.e. close to the reaction chamber. The cells close to the inlet differentiate faster, because they are exposed to the highest nutrition concentration. The cells downstream are exposed to less nutrition, because some has been consumed by cells upstream. The opposite is the case for the simulations with high background concentration, most distinctly shown by the red curve. There is now too large concentration of the toxic nutrition. Cells upstream consume some of the nutrition, thus more tolerable amounts are left for downstream cells. Cells close to the outlet are therefore healthier, and differentiate faster. Hence the decrease in undifferentiated cells along x.

Thus we have shown that toxic constituents in the differentiation cocktail may inhibit cell differentiation, and that large concentrations of the adipogenic differentiation factors may result in slower cell differentiation and lipid production.

It was discussed in Section 4.2 how the lipid concentration is nearly uniform along the cell layer. However a small increase in the lipid concentration along the cell layer was observed, Fig. 4.4. This could be explained by the red curve of Fig. 4.10, where most undifferentiated cells are observed upstream, thus we would expect most lipids downstream, in the outlet end.

Chapter 5

Discussion & Outlook

The model has explained several phenomena that have been observed in experiments, even though it is a simplified model of only 5 variables. Thus all elements that are not essential for describing the central dynamics of the system have been omitted.

One way to make the model more exact is to model the cell density discretely, instead of the continuous distribution used so far. The cells could then be implemented as e.g. half spheres, which would affect the flowfield. Biochemical reactions could then be derived from the receptor densities on the cell membrane surfaces. However, the much higher refinement of the mesh around the cells would be required, and the computations therefore much heavier.

Another interesting addition to the model would be an implementation of a delay before cells initiate the lipid production. It could be achieved by introduction of a new variable, u_c, that describe the concentration of committed cells, i.e. cells in between the states of undifferentiated and differentiated cells.

In addition, one or more new concentration fields could be implemented. Thus the so-called nutrition concentration field could be split into nutrition and salts needed for both metabolism and differentiation, differentiation factors that induce the differentiation process, and toxins that inhibit the differentiation process.

The reduction from three to two dimensions assumed that the flowfield was invariant in the y-direction ("sideways") in the entire reaction chamber. However, we observed that there was a sideway velocity of up to 14 % the velocity in the x-direction. Therefore, the flowfield used in the 2D model could be changed, so the x-velocity is a bit larger close to the inlet and outlet. Yet there are no indications that this adjustment would give significantly different results.

During the last six months, the ProCell platform has made it possible to investigate the differentiation of adipose-derived stem cells. The most important discovery is the indication of the factor, a molecule used for the autocrine/paracrine signaling process. The new information is a result of the interaction between biologists and physicists, where experiments have been planned on the basis of analysis of previous experiments.

I therefore propose the following experiments:

- The conditioned medium should be analyzed, to find out which of the known solutes of the adipogenic cocktails have been consumed. Similarly, the conditioned medium should be analyzed for selected cytokines to identify the factor. The last point is a big piece of work, and must be done in a big laboratory, where thousands of different substances can be screened for.

- When investigating the effect of mixing conditioned medium in the adipogenic medium, it has been assumed that approximately one half of the important differentiation factors have been consumed in the conditioned medium. Therefore, the differentiation factors have been added to the medium with a concentration of 1.5 times the concentration used in standard adipogenic medium. However, in order to be able to compare experiments with and without added conditioned medium directly, it is necessary to know more about the concentration of differentiation factors in the conditioned medium. Thus a series of experiments should be conducted with different concentrations of differentiation factors in the adipogenic medium to estimate which concentration that makes up for the loss of differentiation factors in the conditioned medium due to consumption.

- Similarly, experiments where the concentration of each of the four individual differentiation factors in the adipogenic medium is changed. Thus we can detect if any of them induce or inhibit cell differentiation, respectively.

With more knowledge about the interaction between adipose-derived stem cells and the solutes in the medium, we will be able to describe the differentiation process even further. Moreover, new experiments will give us more information about the factor, and reduce the number of its possible identities.

The ProCell system has already given us results that could not have been obtained with conventional systems, and I believe that the cooperation between physicists and biologists will let us take advantage of the flow systems and give us many big results in the future.

Chapter 6

Conclusion

New experiments have indicated that the differentiation of adipogenic stem cells into white adipocytes depends on paracrine/autocrine signaling. The transmitter substances is suspected to be a type of cytokine.

The experimental setup has been investigated numerically. Important dimensionless numbers have been calculated, and the flowfield in the microsystem has been computed. Knowing the flowfield, is has been possible to estimate the amount of nutrition available to the stem cells at the bottom of the microchannel. Thus a function describing the entrance height of a particle that has time to reach the cells has been derived.

The flowfield of the system has been implemented in a two-dimensional, that also incorporates the transport equations for two types of solutes. The model was set up with parameter values that allowed each of the processes to work on the same timescale, so the interplay could be observed and described. Later, realistic values of most of the parameters were estimated, thus finishing a model that could be compared to experimental data.

Lastly, the model was used to explain three phenomena, that have been discussed in the ProCell group. Thus we showed that large flowrates might flush the secreted factor away from the cells and thus prevent cell differentiation. Similarly, we showed that the cell seeding density is not important for the differentiation of neighboring cells for the assumptions we have made along the way. Finally, it was demonstrated how solute with toxic properties can inhibit the cell differentiation process.

Appendix A

Entrance height function

The limit entrance height of a particle entering the reaction chamber and reaching the cells by diffusion before being flushed out was considered in Section 2.2. The solution is

$$\begin{aligned} z_0\left(v_{\max}\right) = \frac{h}{2} \pm \frac{1}{2}\Bigg(& h^2 + \frac{(2^{5/3}dh^2l)}{(3dh^4lv_{\max}^2+S)^{1/3}} + \frac{2^{1/3}(3dh^4lv_{\max}^2+S)^{1/3}}{v_{\max}} \Bigg)^{1/2} \\ \mp \frac{1}{2}\Bigg(& 2h^2 - \frac{2^{5/3}dh^2l}{(3dh^4lv_{\max}^2+S)^{1/3}} - \frac{2^{1/3}(3dh^4lv_{\max}^2+S)^{1/3}}{v_{\max}} \\ & \pm \frac{2h^3}{\sqrt{h^2 + \frac{2^{5/3}dh^2l}{(3dh^4lv_{\max}^2+S)^{1/3}} + \frac{2^{1/3}(3dh^4lv_{\max}^2+S)^{1/3}}{v_{\max}}}} \Bigg)^{1/2} \end{aligned} \tag{A.1}$$

where $S = \sqrt{-16d^3h^6l^3v_{\max}^3 + 9d^2h^8l^2v_{\max}^4}$.

The equation has four solutions. Thus the three $\pm$ and $\mp$'s in Eq. (A.1) can be replaced by $\{+,-,+\}$, $\{+,+,+\}$, $\{-,+,-\}$ and $\{-,-,-\}$. The first is the relevant, physical solution, the second is another mathematical solution, and the third and fourth are complex solution, respectively.
Thus the equation should be applied with $+$ instead of $\pm$ and $-$ instead of $\mp$.

Bibliography

[1] Kræftens Bekæmpelse. The danish cancer society. www.cancer.dk, 2012.

[2] Mette Hemmingsen. *Usability and Applicability of Microfluidic Cell Culture Systems*. PhD thesis, DTU, 2012.

[3] Ana G. Cristancho and Mitchell A. Lazar. Forming functional fat: a growing understanding of adipocyte differentiation. *Nature Reviews Molecular Cell Biology*, 12(11):722–734, NOV 2011.

[4] Katarina Blagovic, Lily Y. Kim, and Joel Voldman. Microfluidic perfusion for regulating diffusible signaling in stem cells. *PLoS ONE*, 6(8):e22892, AUG 4 2011.

[5] Y.-H. Hsu, M.L. Moya, C.C.W. Hughes Hughes, S.C. George George, and A.P. Lee. A high throughput microfluidic device for generating multiple human microtissues with perfused capillaries. In *The 15th International Conference on Miniaturized Systems for Chemistry and Life Sciences, μTAS: 2011*, 2011.

[6] Rafael Gomez-Sjoeberg, Anne A. Leyrat, Dana M. Pirone, Christopher S. Chen, and Stephen R. Quake. Versatile, fully automated, microfluidic cell culture system. *Analytical Chemistry*, 79(22):8557–8563, NOV 15 2007.

[7] Peder Skafte-Pedersen. *Microfluidic cell culture systems for real-time studies of cells*. PhD thesis, Technical University of Denmark, 2011.

[8] CollasLab, Phillippe Collas, and Mette Hemmingsen. Experience from work in the collas lab at institute of basic medical sciences, university of oslo.

[9] A Gilman, LS Goodman, JG Hardman, and LE Limbird. *Goodman & Gilman's the Pharmacological Basis of Therapeutics*. New York: McGraw-Hill, 2001.

[10] Emily M. Chandler, Bo Ri Seo, Joseph P. Califano, Roberto C. Andresen Eguiluz, Jason S. Lee, Christine J. Yoon, David T. Tims, James X. Wang, Le Cheng, Sunish Mohanan, Mark R. Buckley, Itai Cohen, Alexander Yu Nikitin, Rebecca M. Williams, Delphine Gourdon, Cynthia A. Reinhart-King, and Claudia Fischbach. Implanted adipose progenitor cells as physicochemical regulators of breast cancer. *Proceedings of the National Academy of Sciences*, 109(25):9786–9791, 2012.

[11] Life Technologies. Media formulation detail display, June 2012.

[12] Søren Vedel. *Solutes and cells - a collection of advection-reaction-diffusion problems in biochips*. PhD thesis, Technical University of Denmark, 2012.

[13] H. Bruus. *Theoretical Microfluidics*. Oxford University Press, Oxford, 2008.

[14] Henrik Bruus. Acoustofluidics 10: Scaling laws in acoustophoresis. *Lab Chip*, 12(9):1578–1586, 2012.

[15] M. E Young, P. A. Carroad, and R. L. Bell. Estimation of Diffusion Coefficients of Proteins. *Biotechnology and Bioengineering*, 22:947–956, 1980.

[16] Constantinos Christodoulides, Claire Lagathu, Jaswinder K. Sethi, and Antonio Vidal-Puig. Adipogenesis and WNT signalling. *Trends in Endocrinology and Metabolism*, 20(1):16–24, JAN 2009.

[17] Rodney Cotterill. *Biophysics, An introduction*. Wiley, 2002.

[18] Ron Milo, Paul Jorgensen, Uri Moran, Griffin Weber, and Michael Springer. BioNumbers-the database of key numbers in molecular and cell biology. *Nucleic Acids Research*, 38(1):D750–D753, JAN 2010.

[19] Jakub Stepanek, Michal Pribyl, Dalimil Snita, and Milos Marek. Microfluidic chip for fast bioassays - evaluation of binding parameters. *Biomicrofluidics*, 1(2), APR-JUN 2007.

[20] *Introduction to Comsol Multiphysics®. Version 4.2a.*

[21] MH Gail and CW Boone. The locomotion of mouse fibroblasts in tissue culture. *Biophysical Reviews*, 10(10):980–993, 1970.

[22] Morgan V. DiLeo, John A. Kellum, and William J. Federspiel. A Simple Mathematical Model of Cytokine Capture Using a Hemoadsorption Device. *Annals of Biomedical Engineering*, 37(1):222–229, JAN 2009.

[23] AC Ferguson-Smith, YF Chen, MS Newman, LT May, PB Sehgal, and FH Ruddle. Regional localization of the interferon-beta 2/b-cell stimulatory factor 2/hepatocyte stimulating factor gene to human chromosome 7p15-p21. *Genomics*, 2(3):203–208, 1988.

[24] The ProCell Project. Unpublished, preliminary experimental results from the procell project. www.nanotech.dtu.dk/procell, 2012.

[25] MK Hellerstein. De novo lipogenesis in humans: metabolic and regulatory aspects. *European Journal of Clinical Nutrition*, 53(1):S53–S65, APR 1999. IDECG Workshop on Lower and Upper Limits of Adaptation to Energy Intake and its Principal Substrates, Carbohydrates and Lipids, FAO, ROME, ITALY, DEC 08-11, 1997.

[26] JD Pullar and AJF Webster. The energy cost of fat and protein deposition in the rat. *British Journal of Nutrition*, 37(3):355–363, 1977.

[27] MS Farvid, TWK Ng, DC Chan, PHR Barrett, and GF Watts. Association of adiponectin and resistin with adipose tissue compartments, insulin resistance and dyslipidaemia. *Diabetes Obesity & Metabolism*, 7(4):406–413, JUL 2005.

[28] EP Cathcart and DP Cuthbertson. The composition and distribution of the fatty substances of the human subject. *Journal of Physiology (London)*, 72(3):349–360, JUL 1931.

[29] FAO. Food energy - methods of analysis and conversion factors. Report of a Technical Workshop, Rome, 3-6 December 2002.